Satellite observations of mesoscale ocean features and copropagating atmospheric surface fields in the tropical belt

Richard Justin Small, Shang-Ping Xie,[1] and Jan Hafner

International Pacific Research Center, School of Ocean and Earth Science and Technology, University of Hawaii, Honolulu, Hawaii, USA

Received 15 July 2004; revised 1 November 2004; accepted 4 January 2005; published 22 February 2005.

[1] Recent studies of air-sea interaction using satellite data have shown a high positive correlation between wind speed and sea surface temperature (SST) over mesoscale ocean features in certain frontal regions. The aim of this study is to determine to what extent mesoscale ocean dynamics modifies the surface wind speed over the global tropics between 40°S and 40°N. Cross-spectral and linear regression methods are used to identify robust relationships between ocean and atmospheric variables. The ocean dynamical features, measured by their sea surface height anomaly (SSHA), affect SST in a manner consistent with advection of the mean temperature gradient by anomalous currents. The response varies from 0.2°C of SST per cm of SSHA near the equator to 0.05°C cm^{-1} at higher latitudes. A remarkably consistent in-phase relationship between SST and wind speed is found over the complete domain. Wind speed response varied from 0.5 to 1.5 ms^{-1} per °C of SST change. This in-phase response of wind speed is consistent with previous studies suggesting that the SST variations cause changes in the vertical exchange of momentum and in the pressure gradient, which alter the wind speed.

Citation: Small, R. J., S.-P. Xie, and J. Hafner (2005), Satellite observations of mesoscale ocean features and copropagating atmospheric surface fields in the tropical belt, *J. Geophys. Res.*, *110*, C02021, doi:10.1029/2004JC002598.

1. Introduction

[2] Basin-scale SST anomalies are often observed to be negatively correlated with the strength of prevailing winds [*Mantua et al.*, 1997; *Okumura et al.*, 2001; *Liu et al.*, 1994]. Over the extratropical North Pacific and Atlantic, negative SST anomalies of the basin scale are a response to intensified westerly winds that increase the latent and sensible heat release from the ocean. Most of the anomalous wind forcing, however, is not induced by the in situ SST changes but is considered to result from internal atmospheric variability [*Frankignoul*, 1985; *Barsugli and Battisti*, 1998] or teleconnection from the tropics [*Alexander et al.*, 2002]. In the tropics, this negative correlation is indicative of a feedback between wind evaporation and SST [*Chang et al.*, 2001; *Xie and Tanimoto*, 1998].

[3] In contrast with the basin-scale relationship, recent studies have shown that SST variability on frontal and mesoscale leads to a positive correlation of wind speed and SST [*Xie et al.*, 2004]. For instance, *Hayes et al.* [1989], *Chelton et al.* [2001], and *Hashizume et al.* [2001] noted that stronger winds were observed over the warm phase of Tropical Instability Waves (TIWs). Similar relationships between SST and wind speed were found to occur in mesoscale features in the Kuroshio [*Nonaka and Xie*, 2003; *White and Annis* [2003] (hereinafter referred to as WA03), Somali current [*Vecchi et al.*, 2004], Antarctic circumpolar current [*O'Neill et al.*, 2003; WA03], Brazil current and Gulf Stream (WA03). These results suggest that on the small scales of the ocean mesoscale, it is the ocean that is forcing the atmosphere, via the impact of the SST on the planetary boundary layer mixing processes and pressure gradients [*Xie*, 2004], as discussed in more detail in section 4.2.1.

[4] These findings give rise to the question of whether the relationship between winds and SST is a robust and general feature of ocean mesoscales. This paper aims to answer this question, and to investigate the origin of the SST variability, using satellite data. The region of analysis is limited by the availability of multiyear microwave imager (cloud-transparent) SST for tropical regions only. (The recent launch of the AQUA satellite with the AMSR-E instrument gives potential to use microwave imager data to study the global ocean. However, only two complete years of data are currently available, too short for the analysis.) The tropical belt between 40°S and 40°N (see Figure 1) has been surveyed since December 1997 by the Tropical Rainfall Measuring Mission (TRMM) satellite, on board which the TRMM Microwave Imager (TMI) detects SST. The analysis here will extend the above studies, to include variability over the major ocean basins equatorward of 40° using multiyear data sets.

[5] The variables to be studied here are the sea surface height anomaly (SSHA), the SST, and the wind speed. The relationship between SSHA and SST is shown to indicate how ocean dynamics is related to the surface temperature

[1] Also at Department of Meteorology, School of Ocean and Earth Science and Technology, University of Hawaii, Honolulu, Hawaii, USA.

0148-0227/05/2004JC002598$09.00

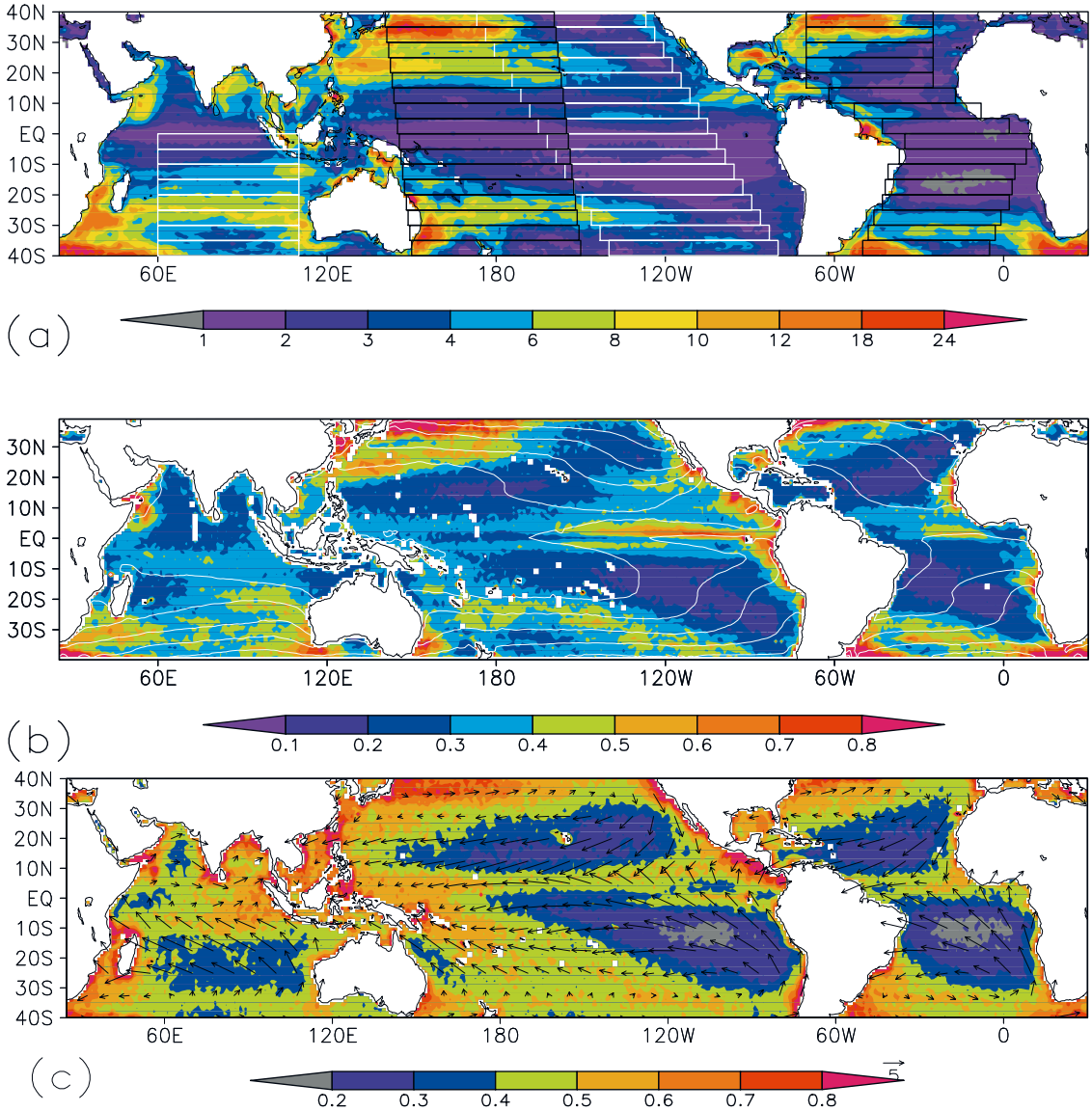

Figure 1. Standard deviation of ocean and atmospheric variables, filtered as discussed in section 2.1. (a) Sea surface height anomaly (SSHA) (color, cm) from October 1992 to August 2001. Overlaid are the 5° latitude boxes making up the south Indian Ocean (white grid), west Pacific (black grid), east Pacific (white grid, overlapping), and Atlantic (black grid) domains. (b) Sea surface temperature (SST) (color, °C), from TRMM TMI, from December 1997 to March 2003. Overlaid is the mean SST from the same period, at intervals of 3°C. (c) Wind speed (color, ms^{-1}), from QuikSCAT, 21 July 1999 to March 2003. Overlaid are the mean wind vectors (ms^{-1}).

variability. In general, the SST field is influenced by surface heat fluxes (sensible and latent), short and long wave radiation fluxes, and mixing and advection in the ocean. For the relatively short, propagating oceanic features being considered in this paper, it is expected that SST change will be governed either by advection of mean SST by eddy currents, or by entrainment from the thermocline into the mixed layer when the thermocline is shallow [*Hill et al.*, 2000].

[6] These two effects governing the relationship of SSHA and SST can be distinguished by studying the phase difference between the two quantities, as discussed in section 4.1.1. Previous studies have shown some conflicting results. For instance, WA03 found that SST and SSHA were collocated in the eddies of their study, based on an analysis of a limited number of snapshots. *Polito et al.* [2001] investigated Tropical Instability Waves and found SSHA led the SST by 90° (in a narrow 2° latitude band) and used this to infer that advection of mean SST dominated SST variations. This contrasted with previous results showing SST led SSHA by up to 90°, in the analysis of tropical Rossby waves by *White* [2000], and an analysis of south Indian Ocean waves by *Quartly et al.* [2003]. In the present study we will provide robust estimates of the relationship between the two variables from the multiyear data sets.

[7] The paper is organized as follows. Section 2 presents the data sets and methods. In section 3 the standard deviation of the mesoscale features are analyzed, in fields of SSHA, SST and in wind speed, to identify the key regions of variability. Section 4 presents the characteristics of multiyear air-sea interaction as determined from linear regression and cross-spectral methods. Section 5 contains a discussion of the results and Section 6 gives the conclusions.

2. Data and Methods

2.1. Satellite Data

[8] This study uses the TMI SST (version 3a) available from December 1997, and QuiKSCAT scatterometer vector winds, available since July 1999, processed by Remote Sensing Systems http://www.ssmi.com) onto a 0.25° grid. TMI data is not affected by clouds (except under heavy precipitation) and hence has a significant advantage over infrared radiometers in regions of large cloud cover (such as the stratus decks in the tropical eastern oceans, and the storm track regions). The radar backscatter (or cross section) measured by scatterometers is most directly related to the stress on the ocean surface, which induces the waves detected by the radar. The wind stress is dependent on wind speed, surface current, and near-surface static stability, so that for example, a particular value of wind stress can correspond to different wind speeds under different stability conditions. For this reason the radar cross section is calibrated to equivalent neutral stability winds at 10 m, U_{10n} [*Wentz and Smith*, 1999]. In a comprehensive investigation of collocated QuikSCAT measurements and mooring data from over 100 buoys (buoy data were from the National Data Buoy Center, the TAO array, the Pilot Research Moored Array in the tropical Atlantic and the Japan Meteorological Agency), *Ebuchi et al.* [2002] found that there was no significant dependence of QuikSCAT minus buoy U_{10n} on either SST or on air-sea temperature difference.

[9] Daily output is obtained from a 3 day running mean of data to improve the coverage. We further average the data to produce a weekly data set. In off-equatorial regions this averaging does not significantly degrade the resolution of features of interest (with periods of 100 days or more), but near the equator it may impact on short, 20–30 day period TIWs. However, for general consistency, the weekly average is applied everywhere. (For the TIWs, the results have been validated against analysis at daily resolution where possible).

[10] Sea level data is gathered in the form of combined TOPEX/POSEIDON and European Remote Sensing satellite SSHA from Centre National d'Etudes Spatiales (CNES) Archiving, Validation and Interpretation of Satellite Oceanographic data (AVISO [*Ducet et al.*, 2000]), from October 1992, on a 0.25° grid, every 10 days. (For comparison of SSHA and SST, the SST fields are linearly interpolated in time onto the time of the SSHA output.) The following time periods were studied in the joint analysis: for SSHA and SST, December 1997 to March 2003; for SST and wind speed, July 1999 to March 2003. For analysis of one data set alone, we use the complete data set up to March 2003.

[11] In order to focus on mesoscale variability, a running average over 10° of longitude is removed, as are a running average over 40 weeks and the first three annual harmonics. The domain of interest is determined by the TRMM data coverage and is shown in Figure 1.

2.2. Cross Spectra

[12] In this study spectral Fourier analysis is used to examine waves occurring in different types of satellite data and their relationships. Fourier analysis was chosen as it provides a clear method of summarizing changes in wave characteristics and relationships with latitude. In contrast with the Radon transform [*Hill et al.*, 2000] it has the ability to identify wavelengths and period as well as phase speed. The need here to provide short summaries of wave characteristics precludes the use of finite-impulse-response filters [*Polito and Liu*, 2003] or wavelet analysis [*Cromwell*, 2001], which introduce added dimensions (a time and/or space dependence) into the spectra. Although there are well known limitations of applying fast Fourier transform (FFT) techniques to determine wave characteristics, particularly in respect of nonstationary features, the FFT approach is taken here as our main aim is not to accurately and precisely determine spatial and temporal characteristics (as done by, e.g., *Polito and Liu* [2003] and *Chelton and Schlax* [1996]), but to focus instead on the phase and response relationship between quantities in an overall sense. The validity of this FFT approach is investigated here by comparing against a local analysis performed using linear regression (see section 2.4).

[13] In brief, the cross-spectral analysis technique compares and correlates the Fast Fourier Transforms (FFTs) of two variables. Following the notation of *Emery and Thomson* [1998] (hereinafter referred to as ET98), the quantities used here are the cross-amplitude spectrum $A_{12}(k, \omega)$ (ET98, equation 5.8.13), describing the joint variability for a particular frequency ω and zonal wave number k, regardless of phase relationship; the coherence spectrum $\gamma^2_{12}(k, \omega)$ (ET98, equation 5.8.21), which gives a value between 0 and 1 of the coherence (squared) between two variables; the response function $H_{12}(k, \omega)$ (ET98, equation 5.8.33), which describes the magnitude of the second variable which responds to unit amount of the first variable; and finally the phase spectrum $\Phi_{12}(k, \omega)$ (ET98, equation 5.8.13), describing the phase difference between the two variables of interest. (The convention here is that positive phase difference implies the first array leads the second array.)

[14] It is important to note that in order to get a confident, realistic value of coherence, some smoothing must be applied. The smoothed coherence spectrum is given by

$$\begin{aligned} \gamma^2_{12}(k,\omega) &= \frac{\langle Q(k,\omega)\rangle^2 + \langle Co(k,\omega)\rangle^2}{\langle F_1^*(k,\omega)F_1(k,\omega)\rangle \cdot \langle F_2^*(k,\omega)F_2(k,\omega)\rangle}, \\ Q(k,\omega) &= -\Im(F_1^*(k,\omega)F_2(k,\omega)), \\ Co(k,\omega) &= \Re(F_1^*(k,\omega)F_2(k,\omega)), \end{aligned} \tag{1}$$

where angled brackets denote a smoothing over spectral components, $F_1(k, \omega)$ and $F_2(k, \omega)$ are the Fourier components of the two variables, and $\Im$ and $\Re$ denote imaginary and real parts. Confidence limits can be determined from the number of degrees of freedom in the

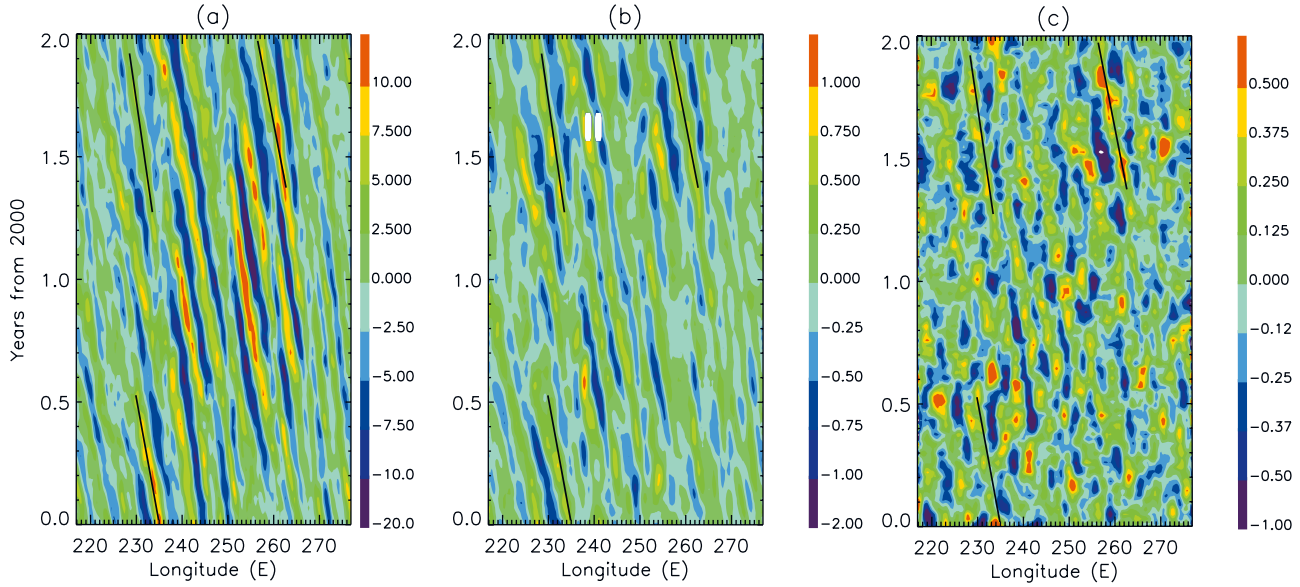

Figure 2. Time-longitude (Hovmoller) plots of filtered data at 35°S, eastern Pacific. (a) SSHA (cm). (b) SST (°C). (c) Wind speed (ms^{-1}). Axes show longitude (°E) and time (years from 2000). Examples of westward propagating features are marked with bold lines in Figure 2a; the lines are reproduced in Figures 2b and 2c.

smoothed spectra. Following ET98, if $(1 - \alpha)$ is the $(1 - \alpha)100\%$ confidence interval we require, then the confidence limit is given by

$$\gamma^2 = 1 - \alpha^{2/(\mathrm{DOF}-2)}. \quad (2)$$

[15] For the analysis presented here, the spectrum is smoothed over a domain of three frequency points by three wave number points, so that there are 18 degrees of freedom (one each for the real and imaginary parts of the complex numbers), so for a 95% confidence limit ($\alpha = 0.05$), $\gamma^2 = 0.31$, while for 99% confidence, $\gamma^2 = 0.44$. (Note that it may be questioned whether the smoothing over adjacent spectral components is a good method of introducing extra degrees of freedom. To test this, the results were compared to an analysis where smoothing spectra from adjacent latitude points was used to introduce extra degrees of freedom. Both methods gave similar results, particularly with respect to the result significance.)

[16] The method is illustrated in Figures 2–4, for a reasonably energetic location of 35°S in the eastern Pacific. Hovmoller plots of the SSHA, SST, and wind speed (Figure 2) show clear westward propagating waves in most of the record. For example, the paths of three of the propagating features of the SSHA of Figure 2a are reproduced in Figure 2b and Figure 2c, and can be seen to correspond to features in SST and wind speed respectively. Power spectra of SSHA and SST give more detail of the scales of the wave activity (Figures 3a and 3b), and confirm the dominance of energy in westward propagating waves. The power spectrum peaks are closely located in wave number frequency domain and are overlaid in Figure 4a. The cross-amplitude spectrum (Figure 4b, shaded) shows a clear, single peak located around ($k = 2.2 \times 10^{-1}$ deg^{-1}, wavelength = 414 km, $\omega = 5 \times 10^{-3}$ $days^{-1}$, period 200 days. Note the convention here that the positive wave number and frequency denotes a westward moving wave.) The phase difference (Figure 4b, white contours) at that location is between −30° and −40° so in this case the SST is leading the SSHA. The cross-amplitude spectrum is overlaid on the coherence squared in Figure 4c: it demonstrates that the cross-amplitude peak is associated with highly significant γ^2_{12} values of over 0.92 (the 99% significance value was 0.44). The response function of SST to SSHA associated with the cross-amplitude peak is H_{12} = 0.07–0.08°C cm^{-1} (Figure 4d).

2.3. Mapping the Cross-Spectral Results

[17] For convenience, the tropical area under consideration is divided into four subdomains, as shown in Figure 1a. The Pacific Ocean, having a larger area, includes one domain for the east and one for the west, to help separate out western and eastern processes. The narrower Atlantic and south Indian Oceans are each given one domain. (The Indian ocean north of the equator is not considered as much of it is contained within two smaller seas (Arabian Sea and Bay of Bengal) which have different wave characteristics and are rather narrow for an individual analysis.)

[18] The spectral analysis is performed as follows. Taking the eastern Pacific domain as an example, for each latitude within the domain (40°S to 40°N, at 0.25° spacing (in many cases, data gaps were found within 5° of the north and south domain of the TRMM data; for that reason, coherence results are typically only shown from 35°S to 35°N)), a longitude-time map is produced. A Hanning window is applied in longitude and time to both fields. Then an FFT is applied to each data set, and from this the cross-spectral method described in section 2.2 is applied. From this data, the location of the peak cross-amplitude value of westward propagating waves is determined, along with the associated wave number, frequency, cross amplitude, coherence,

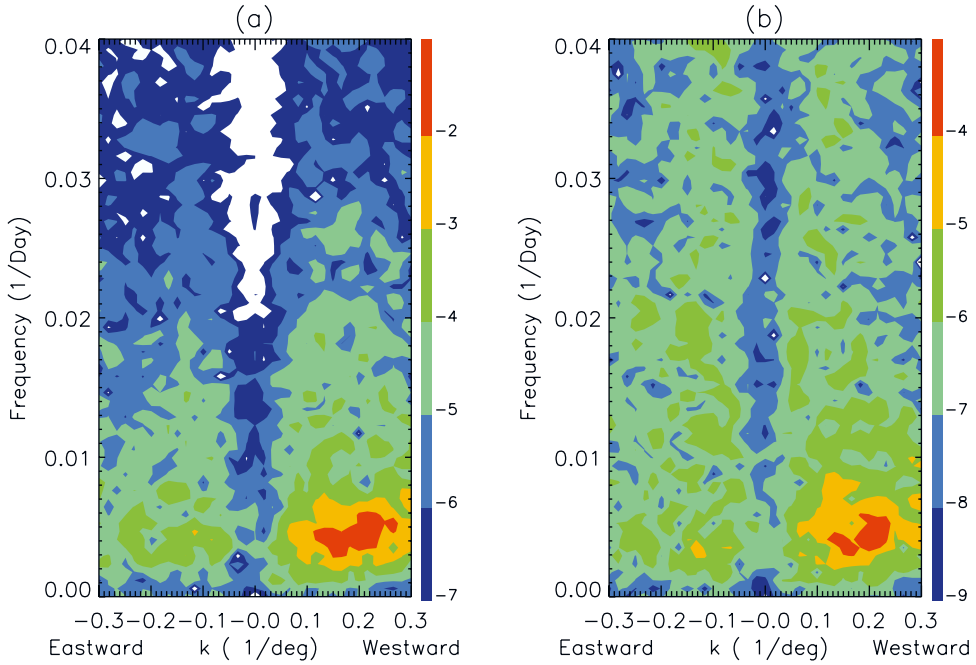

Figure 3. Power spectra for filtered data: (a) SSHA (cm^2, log_{10} units) and (b) SST ($°C^2$, log_{10} units). Note the convention that positive wave numbers denote westward moving. Eastern Pacific, 35°S. Blank areas fall below color bar values.

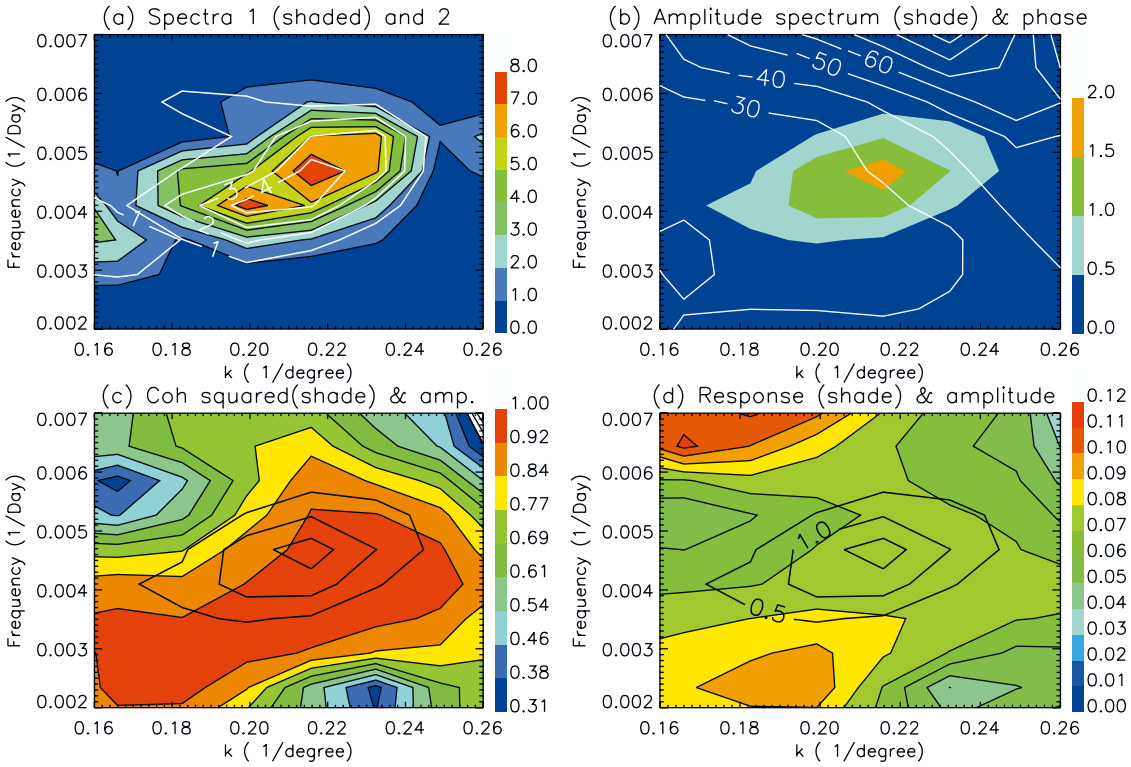

Figure 4. Cross-spectrum results for SSHA and SST, 35°S, eastern Pacific shown in Figure 1. (a) Power spectrum of SSHA (10^{-2} cm^2, color) and of SST (10^{-4} $°C^2$, white contours). (b) Cross-amplitude spectrum (10^{-5} cm^2 $°C^2$, color) and phase spectrum (degrees, white contours (the negative values denote SST leading SSHA)). (c) Coherence squared (color) and cross amplitude (10^{-5} cm^2 $°C^2$, bold contours, interval 0.5). (d) Response function (color, °C cm^{-1}) and cross amplitude (10^{-5} cm^2 $°C^2$, bold contours).

phase, and response function. (The data set was dominated by westward propagating waves, in agreement with previous results from *Chelton and Schlax* [1996], *Hill et al.* [2000], and many others. For simplicity, we describe only these waves.) Finally, the median from the five degrees of latitude in each box in Figure 1a is applied, to remove isolated spikes. This data is used to produce plots of spectral quantities against latitude.

[19] In addition to the covariability results, a by-product of the spectral analysis is the determination of the characteristic wave number, frequency, and derived phase speed at each latitude in each domain. These results are presented in Appendix A and used for later reference.

2.4. Linear Regression

[20] To supplement the cross-spectral calculations, linear regressions have been performed in some limited regions to confirm and illustrate more clearly the spatial relationships between the ocean and atmospheric variables. The regression describes the relationship between a reference variable (such as SST) at a fixed point, and the variable of interest. Following *Hashizume et al.* [2001], a number of regression maps were compiled with reference points within 2° longitudinally of the central point, then a composite compiled by taking the mean of each map with the reference points matched. This was done to remove a small amount of noise in each individual map. The linear regressions are performed using 3 years of weekly data, from mid-July 1999 to mid-July 2002. The results of the local regression analysis are generally consistent with those of the global spectral analysis (section 4).

3. Spatial Patterns of Standard Deviation

[21] In this section the variability of each individual component under consideration (SSHA, SST and wind speed) is discussed, in order to determine where the most energetic mesoscale features occur. Results are presented in terms of the temporal standard deviation over the full record of each component, filtered in time and space.

3.1. Sea Surface Height Anomaly (SSHA)

[22] Figure 1a shows the SSHA standard deviation across the tropical belt of interest to this study, derived from 10.5 years of data (October 1992–March 2003). The standard deviation plot allows identification of the main regions of ocean mesoscale activity which will be studied in detail in the next section. The features in Figure 1a confirm and extend the analyses of *Stammer* [1997] and *Ducet et al.* [2000], the latter based on the first 6 years of merged TOPEX/POSEIDON and ERS satellite data.

3.1.1. Pacific Ocean

[23] In the North Pacific, two main bands of high standard deviation (σ) extend eastward from the western boundary, centered on 22°N ($6 < \sigma < 18$ cm) and 30°–35°N ($12 < \sigma < 24$ cm). The northern band is associated with the Kuroshio/Kuroshio Extension (KE) and the southern one with the Subtropical countercurrent (STCC [*Qiu*, 1999]) and the Hawaiian Lee countercurrent (HLCC [*Xie et al.*, 2001; *Kobashi and Kawamura*, 2001]) west and east of the Dateline, respectively. A weaker band ($3 \text{ cm} < \sigma < 6$ cm) centered around 7°N near the western boundary is associated with the north equatorial current (NEC)/north equatorial countercurrent (NECC). In the South Pacific, a broad region of moderate standard deviation ($3 < \sigma < 9$ cm) extends eastward from the eastern Australia coast across most of the basin, between 20° and 30°S in the west and then tilting southeastward to a meridional extent of 30° and 40°S in the east; at the far west at least the standard deviation is partly due to east Australian current eddies ($12 < \sigma < 24$ cm). This broad band across the Pacific Ocean is referred to here as the South Pacific Waveguide, and is also related to the south tropical countercurrent of *Merle et al.* [1969] and *Qiu and Chen* [2004]. Note that the variability in this region and others discussed later may be due either to instabilities of the mean state, or due to propagation of free waves (both introducing temporal variance). This paper does not aim to distinguish between the possible causes of SSHA variability, and the zonally elongated zones of high variability will be referred to as waveguides, with the caveat that instability may also be contributing to the variance.

[24] In the central Pacific, a local maximum ($3 < \sigma < 6$ cm) of a few degrees latitudinal extent centered around 5°N is due to TIWs [*Legeckis*, 1977] on the northern edge of the Cold Tongue. (There is also a weaker signature of TIWs at 5°S on the southern edge of the Cold Tongue, not visible in Figure 1a). In the eastern Pacific, moderate standard deviation ($3 < \sigma < 9$ cm) regions are located close to the coast associated with the California current off North America and the Humbolt current off South America, and west of Central America in the vicinity of the Costa Rican Dome [see *Kessler et al.*, 2003] and upwelling regions associated with gap wind jet variability (such as the Gulfs of Tehuantepec [*Chelton et al.*, 2000], Papagayo, and Panama). Across the open Pacific Ocean the standard deviation is low ($\sigma < 3$ cm) between 15°S and the equator.

3.1.2. Atlantic Ocean

[25] In the Atlantic the highest standard deviation can be seen associated with the Gulf Stream (GS) and its eastward extension north of Cape Hatteras ($12 < \sigma < 24$ cm), and the "North Atlantic Waveguide" at 34°N [*Cromwell*, 2001] composed of eddies along the Azores current [*Pingree*, 2002; *Mouriño et al.*, 2003] which extends almost to the European coast; also offshore of the Amazon associated with north Brazil current eddies ($12 < \sigma < 30$ cm) [*Garzoli et al.*, 2004]; and an eastward extension from the South American coast at 5°N ($3 < \sigma < 9$ cm), related possibly to shear between the equatorial currents (NEC, NECC) respectively; in a broad band about 5° latitude wide centered at 30°S spanning the Atlantic ($3 < \sigma < 9$ cm), related to the region of cut-off eddies from the Agulhas retroflection [*Garzoli et al.*, 1999; *Schouten et al.*, 2000] extending down to 40°S near the tip of South Africa (where $12 < \sigma < 30$ cm), referred to here as the South Atlantic Waveguide (previously observed by *Ducet et al.* [2000]); and large standard deviation off Argentina south of 30°S ($12 < \sigma < 18$ cm) associated with the Brazil current and its confluence with the Malvinas current [*Goñi et al.*, 1996].

3.1.3. South Indian Ocean

[26] The southern part of the Indian Ocean exhibits moderate standard deviation ($3 < \sigma < 9$ cm) across the basin between 20° and 30°S. This band, studied by *Morrow and Birol* [1998], appears related to the Leeuwin current

eddies off western Australia, 25°–30°S [*Fang and Morrow*, 2003], propagating westward from their generation point. This band will be referred to here as the South Indian Waveguide. Moderate eddy variability ($6 < \sigma < 9$ cm) is also located just south of the Indonesian arc, centered at 12°S, where *Perigaud and Delecluse* [1992] found evidence of a strong annual Rossby wave, and *Feng and Wijffels* [2002] found strong intraseasonal standard deviation associated with the SEC and the Indonesian throughflow; and the Agulhas retroflection south of 35°S (note the Agulhas and Mozambique currents, associated with $\sigma > 12$ cm, are not included in the covariability analysis below).

3.2. Sea Surface Temperature (SST)

[27] For comparison, the standard deviation of filtered SST and the mean SST is shown in Figure 1b. Many, but not all, of the features seen in SSHA standard deviation in Figure 1a are reproduced in the SST standard deviation. In regions where high SSHA standard deviation coincides with a mean SST gradient, there is high SST standard deviation, suggesting temperature advection by geostrophic currents (e.g., in the Gulf Stream region, and around most of the other western boundary currents, where $\sigma > 0.6$°C. Note that although currents in eddies are roughly in steady geostrophic balance with SSHA, the propagation of the eddies causes variations in time which give rise to the SST variability.) High SST standard deviation ($\sigma > 0.5$°C) is also associated with the STCC, the California current, peaking at 20°N, extending westward in the mean SST gradient, and associated with the gap wind jets off Central America which cause significant upwelling and eddies as discussed above. Further, the broad bands of energy across the ocean basins identified above as the South Indian Waveguide and South Pacific Waveguide are seen in both quantities, where typically $\sigma > 0.4$°C, while the South Atlantic Waveguide in the Atlantic has a more northwest-southeast tilt in the SST field than in the SSHA possibly due to the distribution of mean SST gradient. More notable differences are that the TIW standard deviation is high ($\sigma > 0.5$°C) and dominates the equatorial eastern Pacific and Atlantic Oceans in the SST, at around 2°N (lying along the mean SST fronts), while features such as eddies in the Bay of Bengal and those associated with the HLCC in the North Pacific, the NEC/NECC and SEC in the Atlantic and Indian Oceans have relatively weak signatures in the SST standard deviation due to the weak mean SST gradients there.

3.3. Wind Speed

[28] Next the wind speed standard deviation (Figure 1c) may be compared with the oceanic surface variables (Figures 1a and 1b). The wind speed standard deviation mirrors many of the features seen in the SSHA standard deviation (Figure 1a), and, more particularly, the SST standard deviation (Figure 1b). High standard deviation of wind speed ($\sigma > 0.5$ ms^{-1}) can be seen extending eastward from the major western boundary currents, and at the location of TIWs, and over the southern ocean waveguides, the South Atlantic Waveguide, South Pacific Waveguide, and South Indian Waveguide (but in the Indian Ocean the standard deviation in wind speed is maximum at more southern latitudes (30° to 40°S) than seen in the SST and SSHA standard deviation). The near-coincidence of these features in the SST and wind speed standard deviation suggests that on the scales of interest here, the wind speed is strongly reacting to the oceanic mesoscale features. However some purely atmospheric features are seen in the wind speed map: the ITCZ is marked as an area of high wind speed standard deviation ($\sigma > 0.4$ ms^{-1}), particularly in the Pacific Ocean centered around 5°N. (In fact, some aspects of Figure 1c resemble the distribution of highest precipitation in rainfall climatologies [see, e.g., *Adler et al.*, 2001], suggesting that convective systems are also contributing to the wind speed variability at these length and timescales. However, these convective systems will have very different phase speeds to the ocean mesoscale features and so do not contribute to the joint SST–wind speed variability discussed below.) The standard deviation of wind speed is also high in many coastal areas, and around islands such as the Hawaiian Islands. This coastal variance maximum is due to variability of coastal winds, with a mean speed which weakens toward the shore. Some of this coastal wind variability may be forced by SST variability, but it requires an along-coast filtering to extract, rather than the zonal filter used here. The coastal variability analysis is beyond the scope of this paper.

4. Joint Variability Results

[29] In this section the joint variability of the ocean and atmospheric fields presented in section 3 is discussed. Firstly, the SSHA is related to the SST in section 4.1, and secondly the SST is related to wind speed in section 4.2. In both sections, a brief review of possible physical mechanisms governing the relationships is given before the results are shown.

4.1. SSHA and SST Covariability

[30] The relationship between SSHA and SST is important in determining how the variable of importance to air-sea interaction (SST) is related to the ocean dynamics governed by SSHA. SST signatures of long SSHA waves may arise from two mechanisms: either by compression or stretching of the near surface layer, or by meridional advection of the mean temperature gradient [*Hill et al.*, 2000].

4.1.1. SST Equation

[31] The dominant terms in the equation relating SST and SSHA may be written as

$$\frac{\partial T'}{\partial T} = -\nu' \frac{\partial \overline{T}}{\partial y} + \alpha\eta' - \nu T', \tag{3}$$

where T is the SST, η is the SSH, v is the meridional current, α is the effect of mixed layer depth on the SST through entrainment processes, ν is a linear damping coefficient, overbars denote a time mean, and primes denote the deviation from that mean. Here it is assumed that the dominant mean SST gradients are in the meridional direction (a reasonable assumption for most of the domain (see Figure 1b)). Coefficient α is positive: a negative SSH perturbation implies a shoaling thermocline and a consequent cooling of the SST if the thermocline is shallow enough and entrainment processes are active. A function of ocean mean state, this thermocline feedback is large in the eastern equatorial oceans, the tropical south Indian Ocean, and coastal upwelling regions (see *Wang et al.* [2004] for a review).

[32] The observed relationship between SSHA and SST shown below will be compared with a simple model. Adapting *Killworth and Blundell* [2003, Appendix C] to include the effect of mixed layer depth on the SST, under the assumption of a planar wave form

$$\eta' = \eta_0 \exp(i\theta) \quad T' = T_0 \exp(i\theta), \tag{4a}$$

with $\theta = kx - \omega t$ and geostrophic currents

$$v' = \frac{g}{f}\eta'_x, \tag{4b}$$

where subscripts denote differentiation, and the relationship between SST and SSHA is given by

$$\frac{T_0}{\eta_0} = \frac{-\frac{g}{f}ik\overline{T}_y + \alpha}{\left(-i\omega + \frac{1}{\tau}\right)}, \tag{5}$$

where $\tau = 1/\nu$ is the damping timescale. We may consider the following four special cases.

[33] 1. The advection-dominant case, $\omega\tau \gg 1$:

$$\frac{T_0}{\eta_0} = \frac{g}{f\omega}k\overline{T}_y. \tag{6a}$$

SSHA and SST are in (out of) phase when $\overline{T}_y/f < 0$ ($\overline{T}_y/f > 0$) for westward propagating waves ($k < 0$).

[34] 2. The advection and damping case, $\omega\tau \ll 1$:

$$\frac{T_0}{\eta_0} = -\frac{g}{f}ik\overline{T}_y\tau. \tag{6b}$$

For $k < 0$, the phase of T' compared to η' becomes $\pi/2 \times \mathrm{sgn}(\overline{T}_y)/\mathrm{sgn}(f)$ [*Killworth and Blundell*, 2003].

[35] 3. The mixed layer depth effect dominant case:

$$\frac{T_0}{\eta_0} = \frac{i\alpha}{\omega}. \tag{6c}$$

SST lags SSHA by 90°.

[36] 4. The mixed layer and damping case:

$$\frac{T_0}{\eta_0} = \alpha\tau. \tag{6d}$$

SST and SSHA are in phase.

[37] As seen in Figure 5, $\overline{T}_y < 0$ over most of the Northern Hemisphere oceans. Hence in the majority of the Northern Hemisphere, advection alone (6a) would lead to SST and SSHA in phase, and the addition of damping (6b) would cause SST to lead SSHA. Note also that under the effects of advection (6a) the response will be high near the equator, where $f \rightarrow 0$, and there are large mean temperature gradients $\overline{T}_y$ in the Pacific and Atlantic associated with the Cold Tongues (see Figure 1b).

[38] These theoretical predictions will be compared next with the observed joint variability of SSHA and SST.

4.1.2. Linear Regression

[39] The linear regression results from a few selected areas introduce the observed relationship between SSHA and SST. Here the regression is onto the SST at the locations listed in the caption. Two regional examples, from the KE region and the southern Indian Ocean, serve to illustrate the typical case. In the KE region (Figure 6a), the anticyclone (shading denotes the SSHA) advects cool water southward on its eastern flank, leading to cooling, and warm water northward on its western flank, leading to warming (the SST is shown as contours). In the south Indian Ocean (Figure 6b), the anticyclone advects cool water northward on its eastern flank, leading to cooling, and warm water southward on its western flank, leading to warming. On its own this effect would result in the SST centers overlying the SSHA centers. However, the SST centers in Figures 6a and 6b are found just west of the SSHA centers, as confirmed in the following coherence analysis, showing that SST leads the SSHA for the westward propagating waves, possibly due to the thermal damping mentioned above.

4.1.3. Cross Amplitudes, Response Function, and Coherence

[40] In the eastern Pacific the largest cross amplitudes $A_{12}(k, \omega)$ (Figure 7a, solid line) are in the South Pacific Waveguide, and between 2° and 5°N (TIW), and around 18°–20°N (due to California current eddies and the easternmost influence of the HLCC). In the western Pacific (Figure 7a, dashed line), the highest $A_{12}(k, \omega)$ are in the South Pacific Waveguide, STCC and KE. Negligible cross amplitudes are observed in the Pacific Ocean between 20°S and the equator. In the Atlantic ocean (Figure 8a, solid line), the largest $A_{12}(k, \omega)$ are found in the South Atlantic Waveguide and associated with the GS, and there is a weaker local maximum at 8°N associated with NEC/north Brazil current eddies. (Note that TIWs have a smaller signature in the Atlantic, possibly because of their short development season: June–August [*Hashizume et al.*, 2001]. This may help explain why their signal in SSHA is low (see Figure 1a), and consequently so is the covariability of SSHA and SST.) However, as will be seen below, Atlantic TIWs are prominent in the SST–wind speed covariability, as they contribute significantly to equatorial SST and wind speed standard deviation, see Figures 1b and 1c.) The highest $A_{12}(k, \omega)$ in the south Indian Ocean (Figure 8a, dashed line) lie in the South Indian Waveguide, and minimum values lie close to the equator. The coherence spectrum associated with these dominant features is high (0.7–0.9) and significant at 99% (Figures 7b and 8b).

[41] Both the response function and the phase difference change markedly around 10° from the equator. The response function H_{12} is typically largest near the equator at around 0.25°C cm^{-1} (Figures 7c and 8c, solid lines) in the Pacific and Atlantic Oceans, due to the small f and high $|\overline{T}_y|$ just off the equator (Figure 5a), as discussed above. Poleward of 10° of the equator the response is smaller and between 0.05 and 0.1°C cm^{-1} in the Pacific and Atlantic oceans (Figures 7c and 8c, solid lines). In contrast the response function in the Indian Ocean changes little with latitude and remain around 0.05°C cm^{-1} (Figure 8c, dashed line). (Note that in the Indian Ocean the equatorial region exhibits a minimum in magnitude of $\overline{T}_y$(Figure 5a), in contrast to the case in the Pacific and Atlantic, and this may counteract any

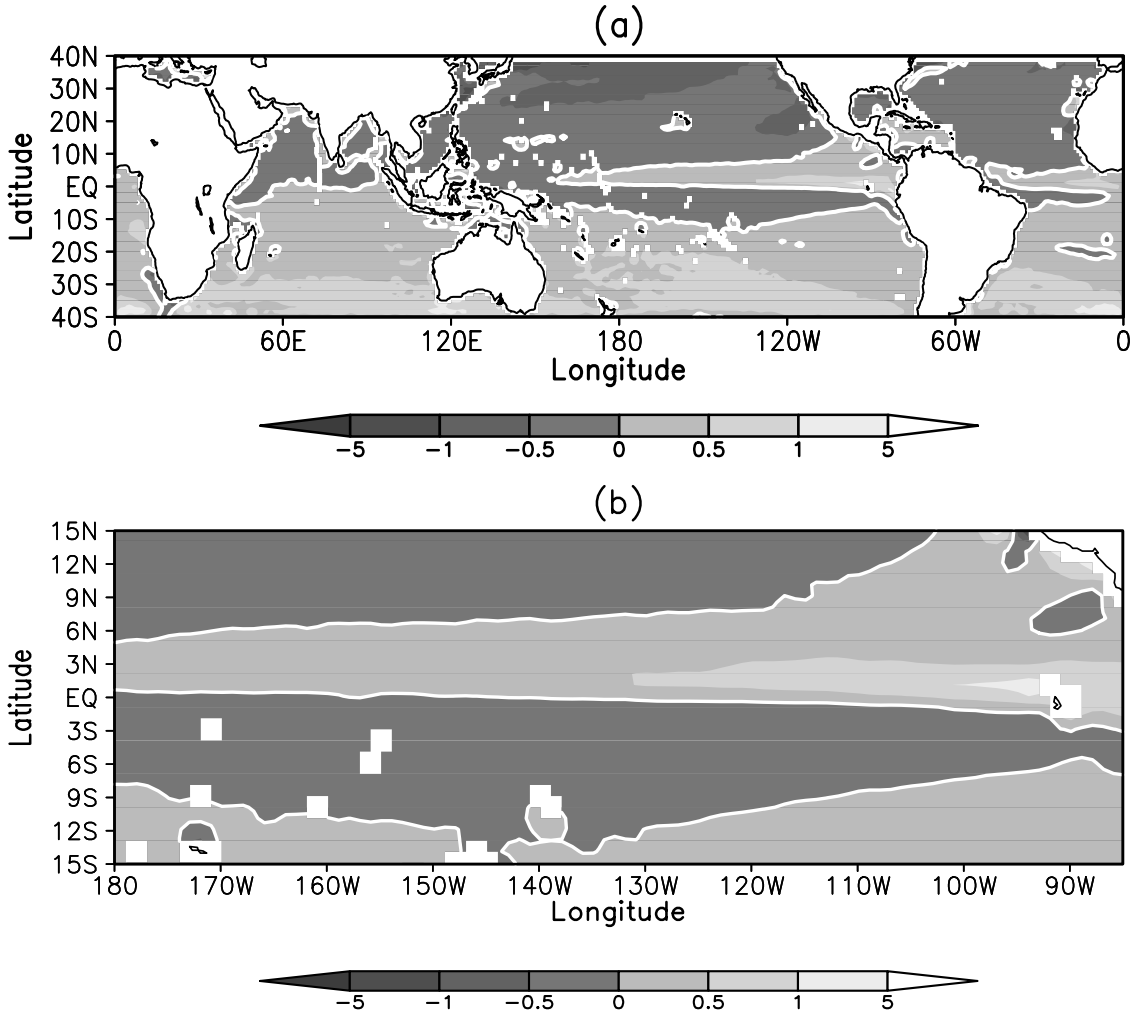

Figure 5. Meridional gradient of mean SST, from the data set in Figure 1b, in units of 10^{-5} °C m^{-1} (approximately °C per degree of latitude). The bold white line marks the zero contour. (a) Distribution from 40°S to 40°N. (b) Eastern tropical Pacific.

influence of the large geostrophic currents in this region of small value of *f*. The response functions derived from the cross-spectral analysis (Figures 7c and 8c) are generally consistent with those derived from linear regression (Figure 6; note that the reciprocal of the regression should be compared with the spectral analysis as the regression is SSHA onto SST). Precise differences between the methods arise from the narrow band nature of the spectral method and the broad band nature of the regression method.)

4.1.4. Phase Difference

[42] The phase difference function Φ_{12} (Figures 7d and 8d) shows many interesting features. For instance, around 10° latitude the phase difference in the east Pacific changes dramatically (Figure 7d, solid line), from SSHA leading SST equatorward of 10° to SST leading SSHA poleward of 10°. This is consistent with the influence of advection and damping (case 2 of section 4.1.1) which predicts that the phase difference is $\pi/2 \times \mathrm{sgn}(\overline{T}_y/f)$, which is positive close to the equator and then changes sign somewhere between 6° and 10° both north and south of the equator in the east Pacific (see Figure 5b, and see also Figure 6c). (Note that when the damping is weak, the advection mechanism predicts an out-of-phase relation in the region where $(\overline{T}_y/f) > 0$, similar to the value observed at 7°N in Figure 7d.)

[43] In the high southern latitudes of the east Pacific (Figure 7d, solid line), the phase varies between −10° and −40° (i.e., SST leads SSHA). Between 15° and 20°N the difference is between −90° and −80°, and at higher northern latitudes it lies between −50° and 0° (SST leads SSHA). The phase difference results outside of the equatorial region are consistent with the advection and damping argument, with SST leading SSH in regions of $\overline{T}_y/f < 0$. The phase difference results in this region are also consistent with the linear regressions of Figures 6a and 6b.

[44] The phase difference results from the other regions (Figures 7d and 8d) also follow the trend of SSHA leading SST in the equatorial region, switching to SST leading in higher latitudes. In the western Pacific and the Atlantic Ocean this is again consistent with the advection and damping mechanism, as the sign of $\overline{T}/f$ changes a few degrees off the equator (Figure 5). In the south Indian Ocean the higher latitude results are consistent with advection and damping, but the fact that SSHA leads SST at 2°S is more consistent with mixed layer and

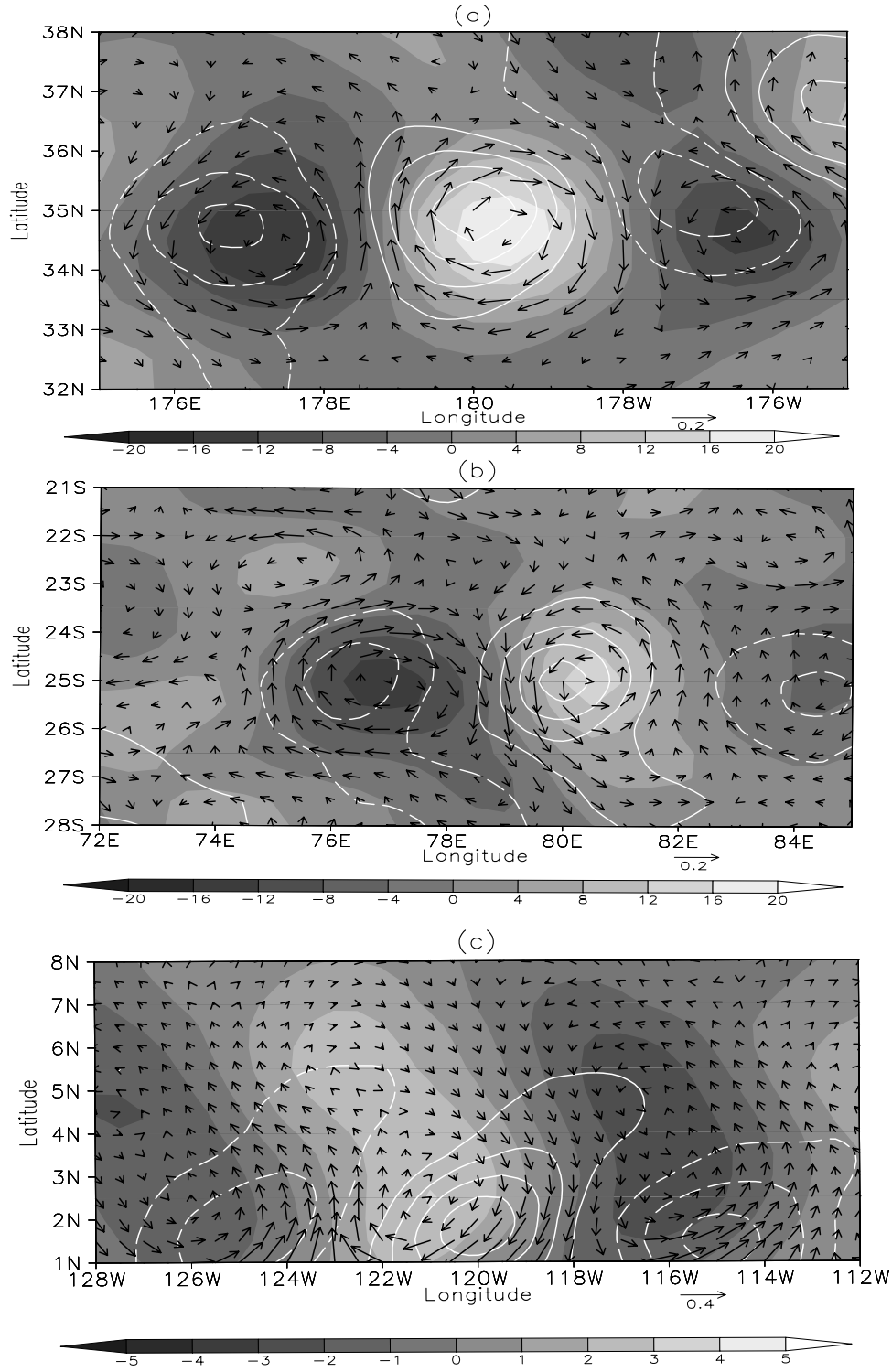

Figure 6. Linear regressions of SSHA and SST onto SST at a fixed point. SSHA (cm $°C^{-1}$, shaded) and geostrophic velocity (ms^{-1} $°C^{-1}$). For reference the SST field is shown as white contours, 0.2 interval, negative values dashed and zero contour omitted. (a) Kuroshio Extension region, reference point 180°E, 35°N. (b) South Indian Waveguide, reference point 80°E, 25°S. (c) Tropical Instability Waves, reference point 2°N, 120°W. Note that the major extrema of the regressed fields were significant at 95% in a student *t* test of the linear regression.

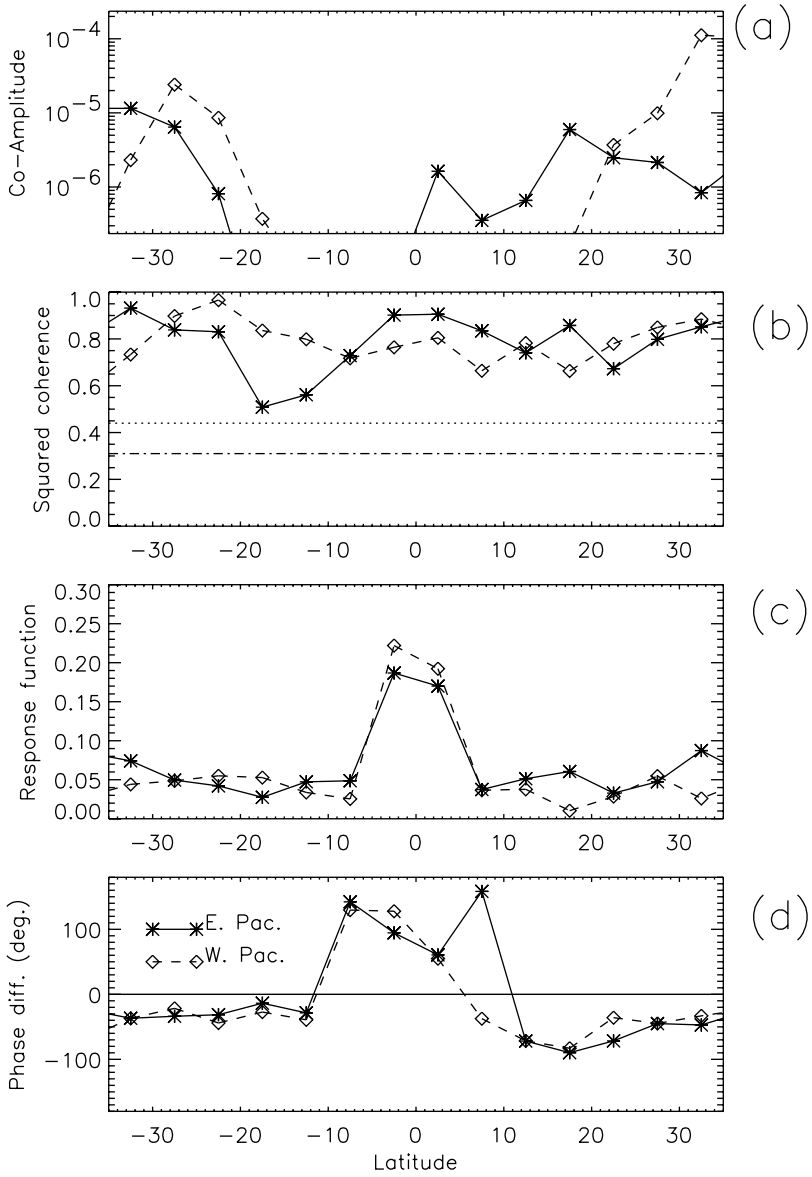

Figure 7. Characteristics of the peak in the cross spectrum of SSHA and SST as a function of latitude. East Pacific (solid lines with asterisks) and west Pacific (dashed lines with diamonds). (a) Cross amplitude (cm^2 $°C^2$). (b) Squared coherence. Here the dotted line shows the 99% confidence level, and the dash-dotted line shows the 95% level. (c) Response function (°C cm^{-1}). (d) Phase function (degrees (positive values denote SSHA leads)). For reference the zero phase difference is marked as a bold line.

damping effects (cases 3 and 4 of section 4.1.1), as the sign of $\overline{T}/f$ is negative.

4.2. SST and Wind Speed Covariability

4.2.1. Momentum Budget

[45] The dominant terms in the planetary boundary layer momentum budget for the wind velocity vector $\underline{u} = (u, v)$ may be written in Cartesian coordinates (x, y, z):

$$\underset{I}{\frac{D\underline{u}}{Dt}} \cong \underset{II}{\underline{u}.\nabla\underline{u}} \cong \underset{III}{-f\underline{k}\times\underline{u}} \underset{IV}{-\frac{1}{\rho_0}\nabla p - \frac{1}{\rho_0}\frac{\partial}{\partial z}\underline{\tau}(z)}, \tag{7a}$$

where p is pressure, $\tau(z) = \rho\overline{\underline{u}'w'}$ is wind stress or momentum flux, $\underline{k}$ is a unit vertical vector, ρ is the air density and ρ_0 a reference value, f is the Coriolis parameter, $\times$ denotes the cross product, and ∇ is the gradient operator. Here term I represents the horizontal advection or advective acceleration, term II the Coriolis force, term III the pressure gradient, and term IV is convergence of the momentum flux (vertical mixing). The budget can be vertically integrated over some suitable depth H (such as boundary layer height):

$$\underset{I}{\frac{1}{H}\int_0^H \underline{u}.\nabla\underline{u}dz} \cong \underset{II}{-f\underline{k}\times\hat{\underline{u}}} \underset{III}{-\frac{1}{\rho_0}\nabla\hat{p}} \underset{IV}{-\frac{\{\underline{\tau}(H)-\underline{\tau}(0)\}}{\rho_0 H}}, \tag{7b}$$

where symbols with hats indicate depth averaged quantities.

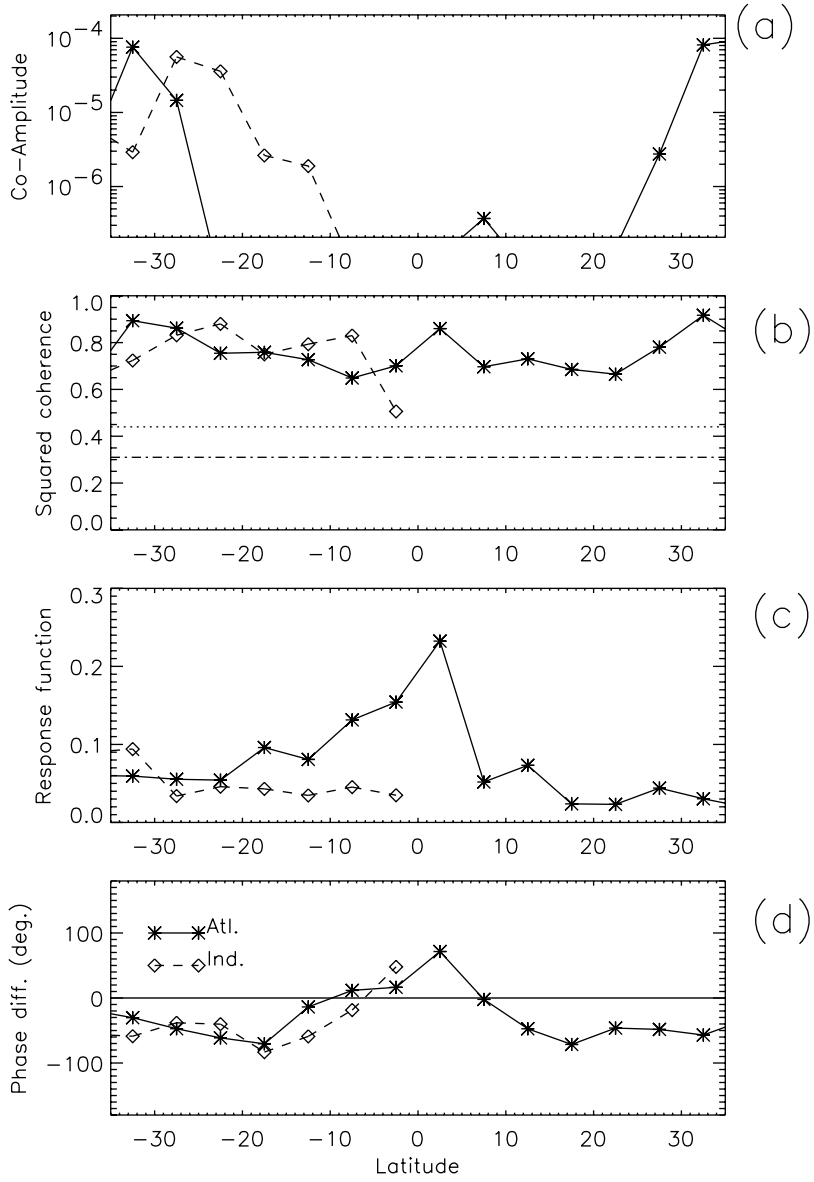

Figure 8. Same as Figure 7, but for the Atlantic (solid lines with asterisks) and south Indian Ocean (dashed lines with diamonds).

[46] *Lindzen and Nigam* [1987] studied the boundary layer response to SST and determined that terms II, III, and IV were most important. By vertically integrating through the boundary layer, linearizing about a mean state, and assuming the stress went to zero at the boundary layer top, they were able to replace term IV with a Raleigh friction ε:

$$\varepsilon \underline{u}' = -f \underline{k} \times \underline{u}' - \frac{1}{\rho_0} \nabla p', \tag{8}$$

where $\varepsilon = C_D|U|/H$, C_D is the drag coefficient, and U is the time mean background wind speed and primes denote deviations from the mean. *Lindzen and Nigam* [1987] also assumed that the air temperature anomaly was proportional to SST anomaly (decaying to 70% of the SST anomaly by 3000 m, the assumed boundary layer depth). Under these assumptions, from (8), it follows that close to the equator ($f \sim 0$), the strongest boundary layer winds would occur over pressure, and hence SST, gradients.

[47] *Wallace et al.* [1989] and *Hayes et al.* [1989] also considered the same terms (II, III, and IV) of (7) to be important in the balance, but believed the momentum flux term did not act just as a simple Raleigh friction. The *Wallace et al.* [1989] argument may be cast in the following form, from (7b):

$$f \underline{k} \times \underline{u}' + \frac{1}{\rho_0} \nabla p' = \frac{\{\underline{\tau}'(0) - \underline{\tau}'(H)\}}{H \rho_0} = -\varepsilon \underline{u}' + K(\mathrm{SST}' - T', \underline{U}), \tag{9}$$

where an extra term K is added to (8) which is a function of sea-air temperature difference (SST-T)$'$ and the profile of

background horizontal wind vector $\underline{U}(z)$, and is related to the transfer of momentum from upper levels to the surface. *Hayes et al.* [1989] used this to explain the case example of TIWs, noting that an easterly jet existed in the upper levels of the planetary boundary layer. When the SST is warmer than air temperature, as observed over the warm phase of TIWs, the environment was unstable, and an exchange of momentum from the upper levels to the surface took place, leading to stronger winds at the surface. In contrast, in a stable situation such as the cold phase of TIWs, the momentum exchange was minimized leading to an enhanced shear between surface and upper level, and consequently surface winds are weak. In this situation the strongest winds would occur over the warmer SST. In the following sections (4.2.2, 4.2.3, and 4.2.4), the results of the cross-spectral analysis of wind speed and SST are compared to these theories, and modifications to the theories above are suggested in section 4.2.5).

4.2.2. Linear Regression

[48] The SST–wind speed relationship is first demonstrated by linear regression of regional examples (Figure 9). Over the KE (Figure 9a), the mean westerly winds (see Figure 1c) are stronger (weaker) over warm (cold) SST, as shown by the regressed wind vectors and the scaler wind speed (shaded). Over the south Indian Ocean (Figure 9b) the wind vector signal is less clear, but the wind speed clearly increases over warm SST and decreases over the cold SST. (Note that although the wind speed response to SST was significant at 95% in a student t test of the linear regression, the wind vectors in the KE and SIW were only marginally significant at 70% over part of the field. This is probably because of changes in background wind direction throughout the year affecting the regressed wind vectors, but not the regressed wind speed.) Over the Tropical Instability Waves in the eastern Pacific (Figure 9c), the mean southeasterly trade winds are enhanced over warm SST and reduced over cold SST, leading to a near in-phase relationship between SST and wind speed. These results are very close to those obtained from a daily analysis for a shorter time period, presented by *Hashizume et al.* [2001], thus giving confidence in the results.

4.2.3. Cross Amplitude, Coherence, and Response Function

[49] Figures 10 and 11 summarize the cross-spectral analysis of SST, featuring many covariations similar to those observed in SSHA-SST. For instance, in the east Pacific (Figure 10a, solid line) there are large cross amplitudes $A_{12}(k, \omega)$ centered around 2°N (due to TIWs), and at the southern (South Pacific Waveguide) limits, and slightly weaker cross amplitudes north of 20°N in the Californian current and HLCC. Negligible cross amplitudes lie between 20° and 5°S. In the western Pacific (Figure 10a, dashed line), largest cross amplitudes are detected in the South Pacific Waveguide and at the northern extreme (KE), with a weaker maximum near the equator due to the westward extension of TIWs. In the Atlantic (Figure 11a, solid line), there is likewise highest covariability at the south and north extremes (South Atlantic Waveguide and GS/North Atlantic Waveguide) and in the TIW belt around 2°N, and in the Indian ocean the covariability is maximum south of 18°S in the South Indian Waveguide (Figure 11a, dashed line). All these maxima are highly coherent, with $\gamma^2_{12}(k, \omega) > 0.8$ (Figures 10b and 11b), significant at 99%.

[50] The response function $H_{12}(k, \omega)$ (Figures 10c and 11c) is around 0.5–0.6 ms^{-1} $°C^{-1}$ at the higher latitudes rising to 1 ms^{-1} $°C^{-1}$ or more close to the equator, with a maximum of 1.7 ms^{-1} $°C^{-1}$ at 8°S in the west Pacific (Figure 10c, dashed line). (Note that the response functions of wind speed to SST shown in the linear regressions of Figure 9 are generally less than that shown in the coherence results. This was found to be because the broad-band regression method smooths and reduces the response relative to the narrow-band spectral method.) Larger response functions would be expected under the *Lindzen and Nigam* [1987] formulation (8) if the air temperature and hence pressure response to changes in SST was large. The air temperature response is a function of the difference between the advective timescale and the timescale for boundary layer heating from the surface. If the advective timescale is much shorter than the heating timescale, air flowing over the SST anomaly will not have sufficient time to respond to the heating, and hence the air temperature response will be small. In general, advective timescales at higher latitudes are smaller than at lower latitudes, because the background wind speeds are typically higher at high latitudes, and the length scale of the mesoscale features is typically smaller (Figure A1a), so that the pressure response is also likely to be smaller at high latitudes. Hence the observations appear to be relatively consistent with a pressure driven response.

4.2.4. Phase Difference

[51] The phase difference between SST and wind speed (Figures 10d and 11d) lies between ±50° over all the domains and is mostly confined to within ±20°. The linear regression examples of Figure 9 confirm the cross-spectral predictions of a near in-phase relationship. This amazingly universal result supports and extends the regional findings of *Chelton et al.* [2001], *Hashizume et al.* [2001], *Nonaka and Xie* [2003], WA03, and *Vecchi et al.* [2004] of wind speed being mostly in phase with SST. This phase relationship between SST and wind speed appears to be consistent with the turbulent exchange of momentum discussed in section 4.2.1 (see equation (9)), since the alternative pressure-driven mechanism of *Lindzen and Nigam* [1987] would imply strongest winds at SST fronts near the equator, 90° out of phase with the observations. However, new findings are suggesting that pressure driving is important as discussed next.

4.2.5. Effect of Thermal Advection and Advective Accelerations

[52] Recently, *Cronin et al.* [2003] and *Small et al.* [2003] have suggested that SLP anomalies are not colocated with SST anomalies in the particular case of TIWs. They found that air-temperature and water vapor anomalies lagged downstream of the SST anomalies, due to the effect of advection by the mean wind, with the air not able to equilibriate with the SST over such small frontal scales. Hence the sea level pressure was lagged downstream of the SST anomalies, and *Small et al.* [2003] found that this was sufficient to cause pressure driven winds to be in phase with SST.

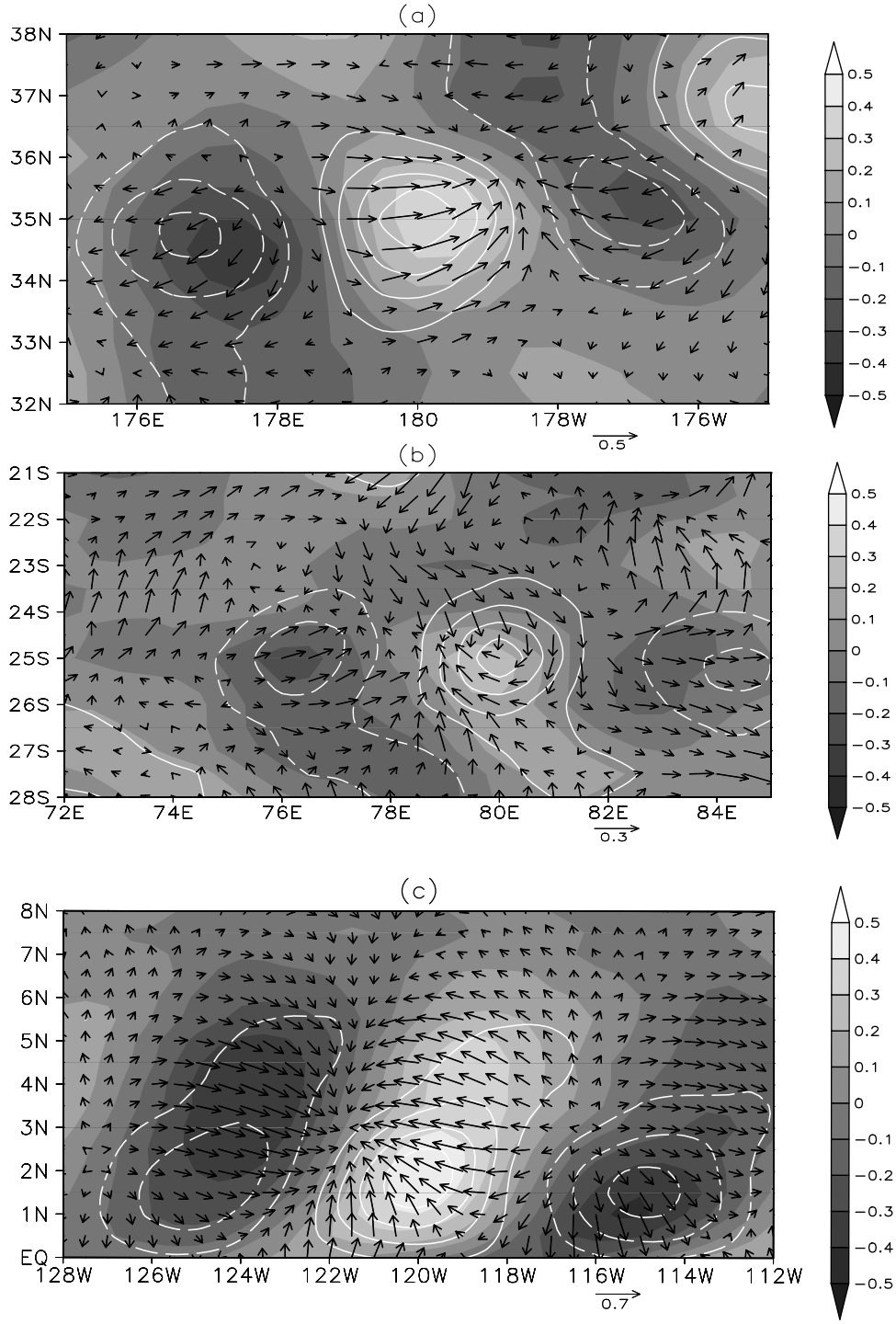

Figure 9. Linear regressions of wind onto SST at a fixed point. Wind speed (ms^{-1} $°C^{-1}$, shaded) and wind velocity (ms^{-1} $°C^{-1}$). For reference the SST field is shown as white contours, 0.2 intervals, negative values dashed and zero contour omitted. (a) Kuroshio Extension region, reference point 180°E, 35°N. (b) South Indian Waveguide, reference point 80°E, 25°S. (c) Tropical Instability Waves, reference point 2°N, 120°W. Note that although the wind speed response to SST was significant at 95% in a student *t* test of the linear regression, the wind vectors were only marginally significant at 70% over part of the field.

[53] It remains to be seen whether the lagged pressure mechanism due to thermal advection contributes to the in phase relationships of SST and wind in higher latitudes where rotational effects may become important, or whether the vertical exchange of momentum due to mixing is responsible. Either way, or maybe under the influence of both, it is a remarkable fact that the observations display a highly uniform phase response of wind to SST over the

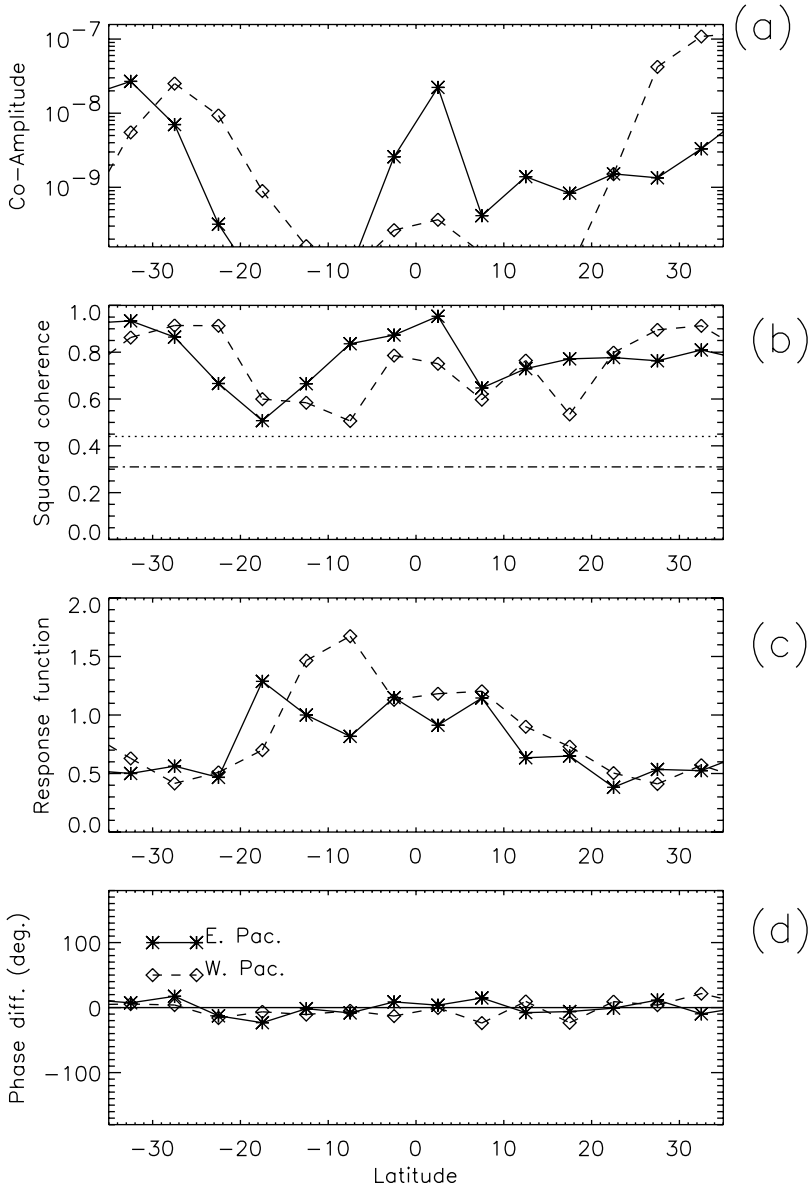

Figure 10. Characteristics of the peak in the cross spectrum of SST and wind speed as a function of latitude. East Pacific (solid lines with asterisks) and west Pacific (dashed lines with diamonds). (a) Cross amplitude ($m^2\ s^{-2}\ °C^2$). (b) Squared coherence. Here the dotted line shows the 99% confidence level, and the dash-dotted line shows the 95% level. (c) Response function ($ms^{-1}\ °C^{-1}$). (d) Phase function (degrees (positive values denote SST leads)). For reference the zero phase difference is marked as a bold line.

whole tropical region for mesoscale time and space scales.

5. Discussion

[54] An interesting question related to this study is to what extent ocean currents affect the QuiKSCAT stress measurements. *Kelly et al.* [2001] and *Thum et al.* [2002] suggest that surface currents can have an effect on the measured stress from scatterometer, and hence the derived 10 m neutral wind speeds. The equatorial region where TIWs occur is likely to be a primary area where this affect is important, as the equatorial currents are strong ($0.5-1\ ms^{-1}$) but the wind speeds are light ($<10\ ms^{-1}$). In higher latitudes the current effect is likely to be masked due to the much stronger winds ($10-20\ ms^{-1}$). The wind speed response to SST measured by QuikSCAT is typically only O($0.1\ ms^{-1}\ °C^{-1}$) (Figures 10c and 11c) and this is comparable with typical current speeds, and so the effect of currents cannot be ignored. However, the positive correlation between SST and near-surface wind speed has also been observed in several in situ data sets over mesoscale ocean features in some regional examples: *Hayes et al.* [1989] in buoy measurements of TIWs; *Nonaka and Xie* [2003] in buoy measurements in the KE region; and in shipboard measurements in the Arabian Sea by *Vecchi et al.* [2004]. Further,

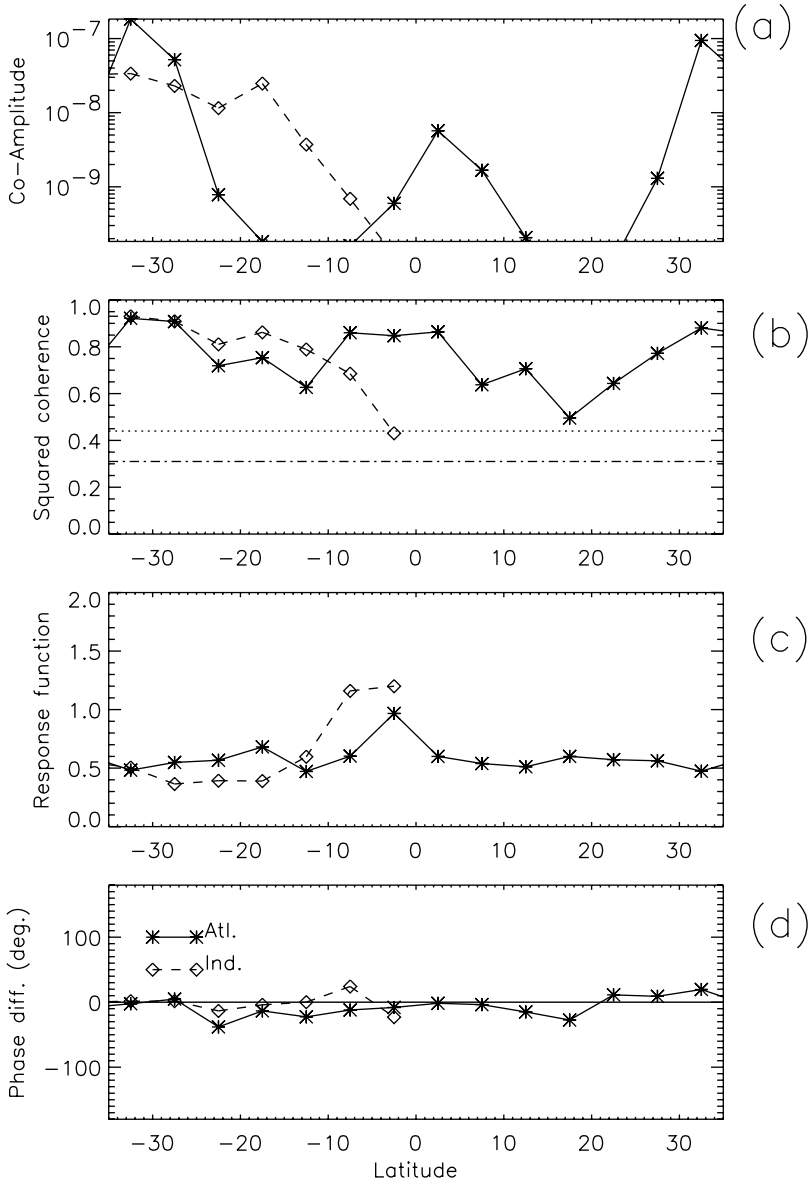

Figure 11. Same as Figure 10, but for Atlantic (solid lines with asterisks) and south Indian Ocean (dashed lines with diamonds).

increased wind speed and wind stress over the warmer water side of ocean fronts has been measured by ship in the Denmark Strait [*Vihma et al.*, 1998], by aircraft over the Gulf Stream [*Sweet et al.*, 1981], and over the Agulhas current [*Jury*, 1994; *Raoualt et al.*, 2000]. This suggests that the qualitative effect of currents on the QuikSCAT measurements of neutral wind does not significantly modify the observed in situ relationship between SST and wind speed. It may also be added that the anomalous scatterometer wind vector response to features such as TIWs [*Hashizume et al.*, 2001] and KE eddies [*Nonaka and Xie*, 2003] generally takes the form of modulations of the wind component in the direction of the background winds, leading to anomalous convergences and divergences (e.g., Figure 9c), but does not take the rotational form which would be expected from the influence of eddying currents. The quantitative effect of the currents on the stress measurements is an area of current and future study.

[55] The results of this paper may be compared with the recent analysis of WA03, who found approximate in-phase relationships between SSHA and SST, and also SST and surface wind, for prevailing westerly wind flow over extratropical mesoscale features (in the GS/KE, Antarctic circumpolar current, and Brazil current region). The present analysis confirms their comparison of SST and wind speed in prevailing westerlies, and extends the results to show that wind speed also varies in phase with SST in easterly trade wind regimes. The present study gives different results to those of WA03 when comparing SSHA and SST: the present results show that, outside of the equatorial region, there is a consistent lead of SST over SSHA by up to one-quarter wavelength. It should be noted that the WA03 results were obtained by spatial analysis of single snapshots,

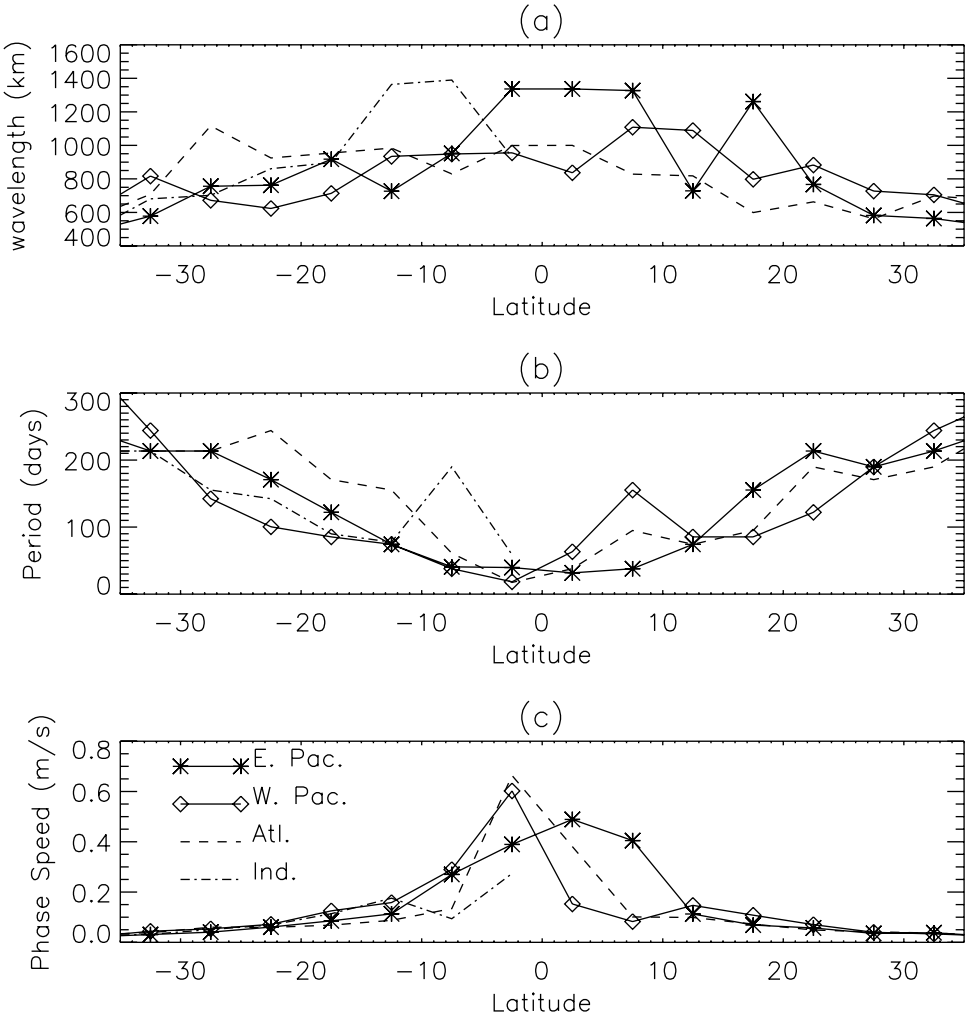

Figure A1. Characteristics of the spectral peak of SSHA as a function of latitude for all four domains (see legend in Figure A1c). (a) Wavelength (km). (b) Period (days). (c) Phase speed (ms^{-1}).

and may be subject to temporal bias, as opposed to the present study investigating spectra obtained from long time series.

[56] The data in this paper has been restricted by the spatial extent of the TRMM satellite. The recent launch of the AQUA satellite with the AMSR-E instrument gives potential to use microwave imager data to study the global ocean. Once long multiyear data sets are available from the satellite, together with the additional data now available from the JASON altimeter, the present study can be extended to cover high-latitude frontal features at high resolution. Preliminary investigations using previously available, lower-resolution data sets by *O'Neill et al.* [2003] and WA03 suggest that the dependence of wind speed on SST in high latitudes is similar to that found in the tropics. In conjunction with the analysis of higher-latitude satellite observations, further modeling studies are required to examine the physical interaction between ocean and atmosphere at these latitudes.

6. Conclusions

[57] Analysis of multiyear, high-resolution satellite data has elucidated the relationship between mesoscale variability in the near surface ocean and the atmospheric response. This study of the tropical belt between 40°S and 40°N focuses on westward propagating waves in the east and west Pacific, the Atlantic and the south Indian Ocean. Cross-spectral and linear regression methods were used in the analysis, which gave generally consistent results. The study resulted in the following conclusions.

[58] Poleward of 10° latitude, where the climatological mean temperature decreases toward the poles, SST leads SSH by between 0° and 90°. These phase results suggest that SST variations are due to meridional advection of the mean temperature gradient. Within 10° of the equator, where the meridional temperature gradient has the opposite sign, the SSH leads SST, also consistent with previous results of advection setting the SST standard deviation. The largest response of SST to SSHA is found near the equator of around 0.2°C cm^{-1}, reducing to less than 0.1°C cm^{-1} at the poleward limits of the domain.

[59] Wind speed response to SST varies from 0.5 to 1.5 ms^{-1} $°C^{-1}$. SST and wind speed vary mostly within ±20° of phase throughout all the ocean basins studied. This remarkable consistency in the phasing of copropagating features in the ocean and atmosphere confirms and extends previous regional analyses. The results indicate that on the

scales of interest here, the ocean forces the atmosphere to give the observed response, which differs from the out-of-phase relationship found by previous researchers for basin-scale climate modes. In particular it is consistent with the vertical mixing of momentum over eddies of differing stability. However, in the TIW region it has also been shown to be consistent with a pressure driven response due a spatial lag between the SST anomaly and the surface pressure anomaly. A definite identification of the physical process involved will require more detailed quantitative comparison between physical models and a combination of satellite and in situ data and extension of this analysis to higher latitudes.

Appendix A: Spectral Scales of Mesoscale Features

[60] The characteristics of the spectral peaks (taken from spectral analysis of the SSHA) for each ocean domain are shown in Figure A1. Typical wavelengths vary from 500 to 1500 km (Figure A1a) and the longest wavelengths are in the equatorial eastern Pacific, due to TIWs, at 17°N offshore of the Californian current region, and in a 5° latitude band centered around 10°S in the Indian Ocean, associated with SEC/Indonesian throughflow eddies (see section 3.) Wave periods (Figure A1b) vary from 30–50 days near the equator to 200–300 days at the higher latitudes (>30° of latitude). The former are due to TIWs, and agree well with previous estimates [e.g., *Legeckis*, 1977; *Contreras*, 2002]. In the Indian Ocean at 7°S the relatively large period of 200 days is again due to the SEC/Indonesian throughflow eddies.

[61] The corresponding phase speeds of the mesoscale waves are shown in Figure A1c. This shows the typical characteristic of phase speed decreasing with increasing latitude, as expected from Rossby wave dynamics [*Killworth et al.*, 1997], from 0.4 to 0.6 ms^{-1} near the equator (except in the Indian Ocean) to less than 0.05 ms^{-1} between 30° and 35°. These values are in general agreement with previous observations [see also *Chelton and Schlax*, 1996; *Polito and Liu*, 2003].

[62] **Acknowledgments.** The TMI data (version 3a) and QuikSCAT data are obtained from the Web site of Remote Sensing Systems, and the altimetry data are obtained from CNES. We would like to thank Dudley Chelton for providing interesting discussion. This study is supported by NASA (grant NAG-10045 and JPL contract 1216010), NOAA (NA17RJ1230), NSF (ATM01-04468), and the Japan Agency for Marine-Earth Science and Technology. This is IPRC contribution 305 and SOEST contribution 6516.

References

Adler, R. F., C. Kidd, G. Petty, M. Morissey, and H. M. Goodman (2001), Intercomparison of global precipitation projects: The Third Precipitation Intercomparison Project (PIP-3), *Bull. Am. Meteorol. Soc.*, *82*, 1377–1396.

Alexander, M. A., I. Blade, M. Newman, J. R. Lanzante, N.-C. Lau, and J. D. Scott (2002), The atmospheric bridge: The influence of ENSO teleconnections on air-sea interaction over the global oceans, *J. Clim.*, *15*, 2205–2231.

Barsugli, J. J., and D. S. Battisti (1998), The basic effects of atmosphere—Ocean thermal coupling on midlatitude variability, *J. Atmos. Sci.*, *55*, 477–493.

Chang, P., L. Ji, and R. Saravanan (2001), A hybrid coupled model study of tropical Atlantic variability, *J. Clim.*, *14*, 361–390.

Chelton, D. B., and M. G. Schlax (1996), Global observations of oceanic Rossby waves, *Science*, *272*, 234–238.

Chelton, D. B., M. H. Freilich, and S. K. Esbensen (2000), Satellite observations of the wind jets off the Pacific coast of Central America. part I: Case studies and statistical characteristics, *Mon. Weather Rev.*, *128*, 1993–2018.

Chelton, D. B., et al. (2001), Observations of coupling between surface wind stress and sea surface temperature in the eastern tropical Pacific, *J. Clim.*, *14*, 1479–1498.

Contreras, R. F. (2002), Long-term observations of tropical instability waves, *J. Phys. Oceanogr.*, *32*, 2715–2722.

Cromwell, D. (2001), Sea surface height observations of the 34°N "waveguide" in the north Atlantic, *Geophys. Res. Lett.*, *28*, 3705–3708.

Cronin, M. F., S.-P. Xie, and H. Hashizume (2003), Barometric pressure variations associated with eastern Pacific tropical instability waves, *J. Clim.*, *16*, 3050–3057.

Ducet, N., P. Y. Le Traon, and G. Reverdin (2000), Global high-resolution mapping of ocean circulation from TOPEX/Poseidon and ERS-1 and -2, *J. Geophys. Res.*, *105*, 19,477–19,498.

Ebuchi, N., H. C. Graber, and M. J. Caruso (2002), Evaluation of wind vectors observed by QuikSCAT/SeaWinds using ocean buoy data, *J. Atmos. Oceanic Technol.*, *19*, 2049–2062.

Emery, W. J., and R. E. Thomson (1998), *Data Analysis Methods in Physical Oceanography*, 634 pp., Elsevier, New York.

Fang, F., and R. Morrow (2003), Evolution, movement and decay of warm-core Leeuwin: current eddies, *Deep Sea Res., Part II*, *50*, 2245–2261.

Feng, M., and S. Wijffels (2002), Intraseasonal variability in the south equatorial current of the East Indian Ocean, *J. Phys. Oceanogr.*, *32*, 265–277.

Frankignoul, C. (1985), Sea surface temperature anomalies, planetary waves, and air-sea feedback in the middle latitudes, *Rev. Geophys.*, *23*, 357–390.

Garzoli, S. L., P. L. Richardson, C. M. Duncombe Rae, D. M. Fratantoni, G. J Goñi, and A. J. Roubicek (1999), Three Agulhas rings observed during the Benguela Current Experiment, *J. Geophys. Res.*, *104*, 20,971–20,985.

Garzoli, S. L., A. Ffield, W. E. Johns, and Q. Yao (2004), North Brazil current retroflection and transports, *J. Geophys. Res.*, *109*, C01013, doi:10.1029/2003JC001775.

Goñi, G., S. Kamholz, S. Garzoli, and D. Olson (1996), Dynamics of the Brazil-Malvinas Confluence based on inverted echo sounders and altimetry, *J. Geophys. Res.*, *101*, 16,273–16,289.

Hashizume, H., S.-P. Xie, W. T. Liu, and K. Takeuchi (2001), Local and remote atmospheric response to tropical instability waves: A global view from space, *J. Geophys. Res.*, *106*, 10,173–10,185.

Hayes, S. P., M. J. McPhaden, and J. M. Wallace (1989), The influence of sea surface temperature on surface wind in the eastern equatorial Pacific: Weekly to monthly variability, *J. Clim.*, *2*, 1500–1506.

Hill, K. L., I. S. Robinson, and P. Cipollini (2000), Propagation characteristics of extratropical planetary waves observed in the ATSR global sea surface temperature record, *J. Geophys. Res.*, *105*, 21,927–21,945.

Jury, M. R. (1994), A thermal front within the marine atmospheric boundary layer over the Agulhas current south of Africa: Composite aircraft observations, *J. Geophys. Res.*, *99*, 3297–3304.

Kelly, K. A., S. Dickinson, M. J. McPhaden, and G. C. Johnson (2001), Ocean currents evident in satellite wind data, *Geophys. Res. Lett.*, *28*, 2469–2472.

Kessler, W. S., G. C. Johnson, and D. W. Moore (2003), Sverdrup and nonlinear dynamics of the Pacific equatorial currents, *J. Phys. Oceanogr.*, *33*, 994–1008.

Killworth, P. D., and J. R. Blundell (2003), Long extratropical planetary wave propagation in the presence of slowly varying mean flow and bottom topography. part II: Ray propagation and comparison with observations, *J. Phys. Oceanogr.*, *33*, 802–821.

Killworth, P. D., D. B. Chelton, and R. A. deSzoeke (1997), The speed of observed and theoretical long extratropical planetary waves, *J. Phys. Oceanogr.*, *27*, 1946–1966.

Kobashi, F., and H. Kawamura (2001), Variation of sea surface height at periods of 65–220 days in the subtropical gyre of the North Pacific, *J. Geophys. Res.*, *106*, 26,817–26,831.

Legeckis, R. (1977), Long waves in the eastern Equatorial Pacific Ocean: A view from a geostationary satellite, *Science*, *197*, 1179–1181.

Lindzen, R. S., and S. Nigam (1987), On the role of sea surface temperature gradients in forcing low level winds in the tropics, *J. Atmos. Sci.*, *44*, 2418–2436.

Liu, W. T., A. Zhang, and J. K. B. Bishop (1994), Evaporation and solar irradiance as regulators of sea surface temperature in annual and interannual changes, *J. Geophys. Res.*, *99*, 12,623–12,637.

Mantua, N. J., S. R. Hare, Y. Zhang, J. M. Wallace, and R. C. Francis (1997), A Pacific interdecadal climate oscillation with impacts on salmon production, *Bull. Am. Meteorol. Soc.*, *78*, 1069–1079.

Merle, J., H. Rotschi, and B. Voituriez (1969), Zonal circulation in the tropical western South Pacific at 170°E, *Bull. Jpn. Soc. Fish. Oceanogr., Professor Uda's Commem. Pap.*, 91–98.

Morrow, R., and F. Birol (1998), Variability in the southeast Indian Ocean from altimetry: Forcing mechanisms for the Leeuwin Current, *J. Geophys. Res.*, *103*, 18,529–18,544.

Mouriño, B., E. Fernández, H. Etienne, F. Hernández, and S. Giraud (2003), Significance of cyclonic SubTropical Oceanic Rings of Magnitude (STORM) eddies for the carbon budget of the euphotic layer in the subtropical northeast Atlantic, *J. Geophys. Res.*, *108*(C12), 3383, doi:10.1029/2003JC001884.

Nonaka, M., and S.-P. Xie (2003), Covariations of sea surface temperature and wind over the Kuroshio and its extension: Evidence for ocean to atmosphere feedback, *J. Clim.*, *16*, 1404–1413.

Okumura, Y., S.-P. Xie, A. Numaguti, and Y. Tanimoto (2001), Tropical Atlantic air-sea interaction and its influence on the NAO, *Geophys. Res. Lett.*, *28*, 1507–1510.

O'Neill, L., D. B. Chelton, and S. K. Esbensen (2003), Observations of SST induced perturbations of the mean wind stress field over the southern ocean, *J. Clim.*, *16*, 2340–2354.

Perigaud, C., and P. Delecluse (1992), Annual sea level variations in the southern tropical Indian Ocean from GEOSAT and shallow-water simulations, *J. Geophys. Res.*, *97*, 20,169–20,178.

Pingree, R. D. (2002), Ocean structure and climate (eastern north Atlantic): In situ measurement and remote sensing (altimeter), *J. Mar. Biol. Assoc. UK*, *82*, 681–707.

Polito, P. S., and W. T. Liu (2003), Global characterization of Rossby waves at several spectral bands, *J. Geophys. Res.*, *108*(C1), 3018, doi:10.1029/2000JC000607.

Polito, P. S., J. P. Ryan, W. T. Liu, and F. P. Chavez (2001), Oceanic and atmospheric anomalies of tropical instability waves, *Geophys. Res. Lett.*, *28*, 2233–2236.

Qiu, B. (1999), Seasonal eddy field modulation of the North Pacific Subtropical Countercurrent: TOPEX/POSEIDON observations and theory, *J. Phys. Oceanogr.*, *29*, 2471–2486.

Qiu, B., and S. Chen (2004), Seasonal modulations in the eddy field of the South Pacific Ocean, *J. Phys. Oceanogr.*, *34*, 1515–1527.

Quartly, G. D., P. Cipollini, D. Cromwell, and P. G. Challenor (2003), Rossby waves, synergy in action, *Philos. Trans. R. Soc. London, Ser. A*, *361*, 57–63.

Raoault, M., A. M. Lee-Thorpe, and J. R. E. Lutjeharms (2000), The atmospheric boundary layer above the Agulhas current during along-current winds, *J. Phys. Oceanogr.*, *30*, 40–50.

Schouten, M. W., W. P. M. de Ruijter, P. J. van Leeuwen, and J. R. E. Lutjeharms (2000), Translation, decay, and splitting of Agulhas rings in the southeastern Atlantic Ocean, *J. Geophys. Res.*, *105*, 21,913–21,925.

Small, R. J., S.-P. Xie, and Y. Wang (2003), Numerical simulation of atmospheric response to Pacific Tropical Instability Waves, *J. Clim.*, *16*, 3722–3740.

Stammer, D. (1997), Global characteristics of ocean variability estimated from regional TOPEX/POSEIDON altimeter measurements, *J. Phys. Oceanogr.*, *27*, 1743–1769.

Sweet, W., R. Fett, J. Kerling, and P. LaViolette (1981), Air-sea interaction effects in the lower troposphere across the north wall of the Gulf Stream, *Mon. Weather Rev.*, *109*, 1042–1052.

Thum, N., S. K. Esbensen, D. B. Chelton, and M. J. McPhaden (2002), Air-sea heat exchange along the northern sea surface temperature front in the eastern tropical Pacific, *J. Clim.*, *15*, 3361–3378.

Vecchi, G. A., S.-P. Xie, and A. Fischer (2004), Ocean-atmosphere covariability in the western Arabian Sea, *J. Clim.*, *17*, 1213–1224.

Vihma, T., J. Uotila, and J. Launiainen (1998), Air-sea interaction over a thermal marine front in the Denmark Strait, *J. Geophys. Res.*, *103*, 27,665–27,678.

Wallace, J. M., T. P. Mitchell, and C. Deser (1989), The influence of sea surface temperature on surface wind in the eastern equatorial Pacific: Seasonal and interannual variability, *J. Clim.*, *2*, 1492–1499.

Wang, C., S.-P. Xie, and J. A. Carton (2004), A global survey of ocean-atmosphere and climate variability, in *Earth Climate: The Ocean-Atmosphere Interaction*, *Geophys. Monogr. Ser.*, vol. 147, edited by C. Wang, S.-P. Xie, and J. A. Carton, pp. 1–19, AGU, Washington, D. C.

Wentz, F. J., and D. K. Smith (1999), A model function for the ocean-normalized radar cross section at 14 GHz derived from NSCAT observations, *J. Geophys. Res.*, *104*, 11,499–11,514.

White, W. B. (2000), Tropical coupled Rossby waves in the pacific ocean-atmosphere system, *J. Phys. Oceanogr.*, *30*, 1245–1264.

White, W. B., and J. L. Annis (2003), Coupling of extratropical mesoscale eddies in the ocean to westerly winds in the atmospheric boundary layer, *J. Phys. Oceanogr.*, *33*, 1095–1107.

Xie, S.-P. (2004), Satellite observations of cool ocean-atmosphere interaction, *Bull. Am. Meteorol. Soc.*, *85*, 195–208.

Xie, S.-P., and Y. Tanimoto (1998), A pan-Atlantic decadal climate oscillation, *Geophys. Res. Lett.*, *25*, 2185–2188.

Xie, S.-P., W. T. Liu, Q. Liu, and M. Nonaka (2001), Far reaching effects of the Hawaiian Islands on the Pacific Ocean atmosphere, *Science*, *292*, 2057–2060.

Xie, S.-P., M. Nonaka, Y. Tanimoto, H. Tokinaga, H. Xu, W. S. Kessler, R. J. Small, W. T. Liu, and J. Hafner (2004), A fine view from space: Report from the 13th Conference on Interactions of the Sea and Atmosphere, *Bull. Am. Meteorol. Soc.*, *85*, 1060–1062.

J. Hafner, R. J. Small, and S.-P. Xie, International Pacific Research Center, School of Ocean and Earth Science and Technology, University of Hawaii, 2525 Correa Road, Honolulu, HI 96822, USA. (jhafner@hawaii.edu; small@hawaii.edu; xie@hawaii.edu)